J. Fluid Mech. (2007), *vol.* 587, *pp.* 97–138. © 2007 Cambridge University Press
doi:10.1017/S0022112007007070 Printed in the United Kingdom

Response of a compressible laminar boundary layer to free-stream vortical disturbances

PIERRE RICCO AND XUESONG WU

Department of Mathematics, Imperial College London,
180 Queens Gate, London SW7 2BZ, UK

(Received 14 June 2006 and in revised form 3 May 2007)

As a first step towards understanding the role of free-stream turbulence in laminar–turbulent transition, we calculate the fluctuations induced by free-stream vortical disturbances in a compressible laminar boundary layer. As with the incompressible case investigated by Leib *et al.* (J. Fluid Mech. vol. 380, 1999, p. 169), attention is focused on components with long streamwise wavelength. The boundary-layer response is governed by the linearized unsteady boundary-region equations in the typical streamwise region where the local boundary-layer thickness δ^* is comparable with the spanwise length scale Λ of the disturbances. The compressible boundary-region equations are solved numerically for a single Fourier component to obtain the boundary-layer signature. The root-mean-square of the velocity and mass-flux fluctuations induced by a continuous spectrum of free-stream disturbances are computed by an appropriate superposition of the individual Fourier components.

Low-frequency vortical disturbances penetrate into the boundary layer to form slowly modulating streamwise-elongated velocity streaks. In the compressible regime, vortical disturbances are found to induce substantial temperature fluctuations so that 'thermal streaks' also form. They may have a significant effect on the secondary instability. The calculations indicate that for a vortical disturbance with a relatively large Λ, the induced boundary-layer fluctuation ultimately evolves into an amplifying wave. This is due to a receptivity mechanism, in which a vortical disturbance first excites a decaying quasi-three-dimensional Lam–Rott eigensolution. The latter then undergoes wavelength shortening to generate a spanwise pressure gradient, which eventually converts the Lam–Rott mode into an exponentially growing mode. The latter is recognized to be a highly oblique Tollmien–Schlichting wave. A parametric study suggests that this receptivity mechanism could be significant when the free-stream Mach number is larger than 0.8.

1. Introduction

Laminar–turbulent transition in a boundary layer is known to be crucially affected by free-stream disturbances. These disturbances generally consist of acoustic, vortical and entropy modes, but they are often loosely referred to as free-stream turbulence (FST) and are usually characterized by a turbulence level Tu (i.e. the root-mean-square value of the velocity fluctuations) and turbulence length scales. A fundamental observation is that the transition Reynolds number strongly depends on Tu (Dryden 1955). It is now generally accepted that at a very low Tu, transition is initiated by the growth of Tollmien–Schlichting (TS) waves, which can be excited by receptivity processes, such as the leading-edge adjustment mechanism (Goldstein 1983) or the interaction of the free-stream disturbances with local and distributed surface roughness (Goldstein & Hultgren 1987). At a moderate Tu, discernible instability waves may still be observed, but their characteristics, e.g. wavelength, frequency and growth rate, are substantially altered. When Tu is relatively high, transition takes the so-called bypass route (Morkovin 1984), without apparently involving TS waves.

1.1. *Bypass transition in incompressible boundary layers*

Experimental studies of transition under the influence of intense FST were first conducted at low speeds by Dryden (1936) and Taylor (1939). They observed that the response of the boundary layer to FST was characterized by spanwise-alternating low- and high-speed regions, which were elongated in the streamwise direction. They suggested that the development of this kind of 'breathing mode' could be a precursor of transition. However, since the experiments of Schubauer & Skramstad (1947), which verified the linear stability theory of Tollmien (1929) and Schlichting (1933), the majority of subsequent studies deliberately focused on boundary layers perturbed by a very low level of FST. The pioneering findings of Dryden and Taylor received little attention until the work of Klebanoff (1971), which revived the interest in this topic and stimulated further work (Arnal & Juillen 1978; Kendall 1985, 1990, 1991; Westin *et al.* 1994). Matsubara & Alfredsson (2001) and Fransson, Matsubara & Alfredsson (2005*b*) conducted detailed measurements of the fluctuations within the boundary layer induced by FST of relatively high level. All the above studies confirmed that fluctuations in the core of the boundary layer consist of predominantly low-frequency components and that the streamwise velocity has a much larger magnitude than both the normal and spanwise velocities. Perturbations of this form thus manifest themselves as streamwise-elongated streaks. They have been referred to as 'Klebanoff modes' in more recent literature.

The visualization experiments of Matsubara & Alfredsson (2001) indicate that streaks may sporadically break down to form turbulent patches or spots. This observation appears to support the suggestion that streaks, once exceeding a certain threshold amplitude, may cause a new form of instability, i.e. streak instability, leading to bypass transition.

The characteristic features of streak development have been reproduced by several recent direct numerical simulations (DNS) of bypass transition (Jacobs & Durbin 2001; Brandt, Schlatter & Henningson 2004; Zaki & Durbin 2005), where FST is modelled by the continuous spectrum of the Orr–Sommerfeld and Squire operators. These simulations indicate that streaks may indeed be unstable, but the detailed breakdown process does not entirely agree with the laboratory observations.

An asymptotic theory describing the entrainment of FST into the boundary layer and the development of the induced streaks has been developed by Leib, Wundrow & Goldstein (1999, referred to hereinafter as LWG). The fact that the relevant perturbations for streak formation are of low frequency and long wavelength means that the streamwise viscous diffusion terms can be neglected. The viscous diffusion and the pressure gradient in the spanwise direction are retained in order to describe typical streaks with spanwise length scale comparable with the boundary-layer thickness. The full Navier–Stokes equations then simplify to the so-called boundary-region equations (Kemp 1951), which may be linearized about the unperturbed base flow if the streaks are of small amplitude. These equations are elliptic in the spanwise direction, but parabolic in the streamwise direction. The latter property gives rise to considerable computational savings since the equations can be solved by marching downstream. The forcing of FST is accounted for by the inhomogeneous conditions imposed at the outer edge of the boundary layer. Using this approach based on the linearized unsteady boundary-region (LUBR) equations, LWG calculated the signature (i.e. the root-mean-square of the streamwise velocity fluctuation) of the streaks induced by FST of a given spectrum. The results show that the boundary layer acts as a filter, allowing low-frequency fluctuations to penetrate into the boundary layer and amplify downstream, while sheltering the high-frequency components. The prediction agrees quantitatively with the measurements, provided that the statistical property of FST is correctly modelled.

An alternative theory for streak development is based on the so-called transient growth (Landhal 1977, 1980). This phenomenon was originally observed for exactly parallel flows such as plane Couette and Poiseuille flows. It refers to the fact that three-dimensional perturbations with very long streamwise wavelengths can experience significant temporal amplification before the final decay. A similar spatial amplification was shown to occur in spatially developing boundary layers (Andersson, Berggren & Henningson 1999; Luchini 2000; Levin & Henningson 2003). Mathematically, the equations governing this kind of perturbation are the steady version of the boundary-region equations as in LWG. The main and significant difference is that in transient growth theory, the disturbances are required to vanish in the free stream, i.e. the forcing from FST is absent. Because the formulation does not take into account any naturally present FST, the upstream condition is usually chosen so as to optimize the perturbation energy at an given downstream location, measured by some rather subjective norm. A perturbation of this kind has been referred to as an ‘optimal disturbance’. However, it is unclear how such disturbances could be driven by FST, or by any actuator in a laboratory setting. By comparison, the formulation of LWG retains all the mathematical ingredients of the transient growth theory, but is more complete in that it properly specifies the naturally present FST. It is thus capable of describing realistically the early stage of streak evolution.

A proper specification of FST is of crucial importance for understanding bypass transition, since the latter is caused by FST in the first place. The key purpose of studying bypass transition is to establish (*a*) the threshold level of FST for bypass transition to occur and (*b*) a quantitative relation between the transition location and the characteristics of FST. It is deemed impossible to achieve those aims of engineering interest through a theory which does not take FST into account.

Predicting or modelling streak development is a first step to understanding bypass transition. The next is to investigate the streak instability, which has been the subject of several numerical and experimental studies. See Brandt *et al.* (2004), Zaki & Durbin (2005) and Fransson *et al.* (2005*a*,*b*) for surveys of recent findings. For the purpose of the present study, it suffices to emphasize that the stability property depends crucially on an accurate description of the streaks. Andersson *et al.* (2001) performed a stability analysis of steady spanwise periodic streaks, which are modelled by optimal disturbances. Their calculation suggests that the threshold amplitude for instability is about 26% of the free-stream velocity, which obviously exceeds by far the amplitude of typical streaks induced by FST. Wu & Choudhari (2003) investigated the stability of unsteady streaks induced by low-frequency vortical disturbances. The spanwise length scale Λ is assumed to be much larger than the local boundary-layer thickness δ^* so that the boundary-layer equations can be used to compute the streak signature. It is shown that streaks of this kind may cause inviscid instability when their amplitude exceeds a critical value, but is still small enough for the linearized equations to be applicable. The inherent unsteadiness is found to be instrumental for such a sensitive effect. The instability of more typical FST-induced streaks with length scale Λ comparable with δ^* poses a more challenging problem. Steps in this direction have been taken by Wundrow (1996) and Wundrow & Goldstein (2001) for steady streaks.

1.2. *Bypass transition in compressible boundary layers*

Unlike the incompressible counterpart, bypass transition in compressible boundary layers remains largely unexplored. A great number of experiments have been conducted primarily to establish the gross correlation between the transition Reynolds number and FST. They showed that the transition position shifts significantly depending on both the FST level (Dryden 1955; Schneider 2001) and the surface roughness (e.g. Pate 1971). However, there exist only a few studies of the detailed physics underlying such correlations.

Laufer (1954) appears to be the first to have investigated the influence of vortical disturbances on compressible boundary-layer transition. He observed that increasing the amplitude of the vortical disturbances causes transition to occur earlier for Mach numbers $M < 2.5$. For $M > 2.5$, the transition location is hardly affected by the amplitude of vortical disturbances. A possible reason for this is that the composition of FST varies with the Mach number. For $M > 2.5$, acoustic disturbances become dominant because the turbulent boundary layers on the tunnel walls radiate a considerable amount of sound (Laufer 1960) to influence the transition over the test model. In general, such facility-produced acoustic noise results in a significantly lower transition Reynolds number in laboratory experiments than that in flight conditions (Schneider 2001). Therefore, prior to possible applications of laboratory data to flight situations, systematic corrections have to be carried out by extrapolating empirical correlations between the transition Reynolds number and relevant parameters characterizing the acoustic disturbances (Stainback 1971). This imperative demand has been the main reason why the majority of experiments have focused on acoustic disturbances while few have considered vortical disturbances.

The experiments of Kendall (1975) provide much information concerning supersonic boundary-layer transition under the influence of high-level FST. A salient feature is that fluctuations over a wide range of frequencies undergo substantial growth. Sufficiently downstream, a peak in the energy spectrum emerges, which corresponds to a Mack I mode in the low-Mach-number supersonic range ($M < 4.5$) (Mack 1984). For higher Mach numbers, a secondary, less pronounced peak representing the Mack II instability was observed to appear. These results indicate that some kind of receptivity mechanism operates in a nominally flat plate to generate instability waves. On the other hand, the broadband amplification cannot be explained by linear instability theory. A forcing theory was proposed by Mack (1975) in order to calculate the boundary-layer response to incident sound waves. Kendall (1975) found that the prediction was in agreement with the measurements in some (but not all) of the cases investigated. He also pointed out that tunnel sound may not be the only disturbances at low speeds and vortical disturbances cannot be excluded.

Demetriades (1989) focused on the transition of a Mach 3 boundary layer, for which the growth of both the Mack I and II modes is weak. Transition appeared to be caused by the continued growth of the forced broadband disturbances. Graziosi & Brown (2002) carried out a thorough investigation of the transition process in a Mach 3 boundary layer, including receptivity, linear instability and onset of turbulence. The dominant boundary-layer fluctuations were of low frequency with the energy being concentrated at the frequencies below the Mack I instability range. The onset of high-frequency disturbances was preceded by spikes in the time traces. The interval between the two successive spikes scaled with the time scale of the low-frequency fluctuations, leading them to speculate that these (acoustically) forced disturbances play an active role in the eventual breakdown into small-scale motions.

Although acoustic disturbances are the main concern in most experimental studies, this does not imply that vortical disturbances are of no relevance. As mentioned above, their influence is significant in the low supersonic speed range ($M < 2.5$) (Laufer 1954; Kendall 1975). In flight conditions, acoustic disturbances are usually weak, at least at locations not dominated by engine-induced noise, and so vortical fluctuations are likely to be the primary external disturbances affecting the transition location.

1.3. *The scope of the present study*

This paper describes how a compressible laminar boundary layer responds to small-amplitude free-stream vortical disturbances of the convected-gust type. It is an extension of the seminal work of LWG to the compressible case. The interest is in predicting the induced fluctuations within the boundary layer and in investigating the compressibility effect and the possible new features that may arise.

As in LWG, the mathematical framework is the linearized unsteady boundary-region equations. In the present compressible case, the energy equation is coupled with the continuity and momentum equations. A physical consequence of this is that vortical disturbances in the free stream, which are of hydrodynamic nature, can generate substantial thermal, i.e. temperature, fluctuations within the boundary layer.

A further aim of the present investigation concerns the receptivity of the boundary layer, i.e. the process through which vortical disturbances generate TS waves. Goldstein (1983) was the first to realize the crucial role of the boundary-layer eigensolutions discovered by Lam & Rott (1960) (see also Ackerberg & Phillips 1972) in triggering exponentially growing TS waves. The key observation is that these eigensolutions undergo wavelength shortening to induce a streamwise pressure gradient. Once the pressure gradient becomes comparable with the inertia in a thin region adjacent to the plate, a decaying Lam–Rott mode evolves into an unstable TS wave. The present paper demonstrates that for three-dimensional disturbances, the boundary-layer equations admit (quasi-) three-dimensional Lam–Rott eigensolutions, which then generate a spanwise pressure gradient. Once this pressure gradient becomes of the same order of magnitude as the inertia in a viscous sublayer, the solution exhibits exponential growth.

The paper is organized as follows. In §2, we formulate the problem. The relevant asymptotic scalings are specified and the resulting flow structure is described. In §3, we consider the flow relatively close to the leading edge, where the boundary-layer equations apply. In §4, we analyse the region further downstream where the unsteady flow is governed by the boundary-region equations. These equations are solved for a single Fourier component of FST. The property of the solution depends on the scaled spanwise wavenumber κ. For κ greater than a critical value κ_c, the fluctuations decay after reaching their peak value. However, for $\kappa < \kappa_c$ they undergo exponential growth. We show in §5 that the growing disturbances are highly oblique TS waves, which are generated through the receptivity mechanism described above. In §6, the result for a single Fourier component is generalized to the case of a broadband FST. The root-mean-square (r.m.s.) values of the velocity and mass-flux fluctuations are computed. A brief conclusion is given in §7.

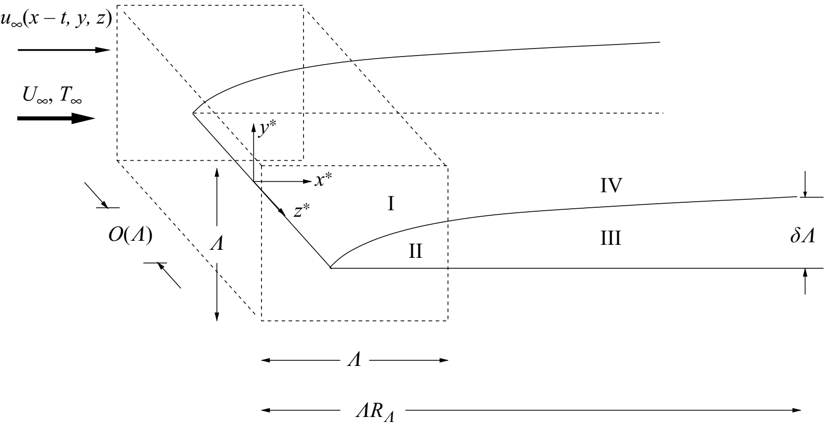

FIGURE 1. Sketch of the flow domain illustrating the asymptotic structure (LWG).

2. Formulation: scaling and asymptotic structure of flow domain

We consider an air flow of uniform velocity U_∞ and temperature T_∞ past an infinitely thin flat plate. Superimposed on U_∞ are homogeneous statistically-stationary turbulent vortical fluctuations. These perturbations are of the convected gust type, i.e. they are passively advected by the mean flow. The air is treated as a perfect gas so that the sound speed in the free stream $c_\infty = \sqrt{\gamma \mathscr{R} T_\infty}$, where $\gamma = 1.4$ is the ratio of the specific heats, and $\mathscr{R} = 287.05$ N m kg^{-1} K^{-1} is the universal gas constant. The Mach number,

$$M \equiv U_\infty / c_\infty,$$

is assumed to be $O(1)$. The wall is taken to be adiabatic.

The formulation follows closely that of LWG. The flow is described in terms of a Cartesian coordinate system (see figure 1), in which a point is represented by a position vector $\boldsymbol{x} = x\hat{\boldsymbol{i}} + y\hat{\boldsymbol{j}} + z\hat{\boldsymbol{k}} = x_1\hat{\boldsymbol{i}} + x_2\hat{\boldsymbol{j}} + x_3\hat{\boldsymbol{k}}$, where x, y and z (or equivalently x_1, x_2 and x_3) define the streamwise, wall-normal and spanwise directions, respectively. They are non-dimensionalized by Λ, the spanwise integral length scale of FST. In the special case of a single Fourier component, Λ is taken to be the spanwise wavelength of the disturbance. All the fluid properties, such as density and dynamic viscosity, are non-dimensionalized by their respective constant values in the free stream, namely ρ_∞ and μ_∞. The velocities and temperature are made dimensionless by U_∞ and T_∞, respectively, and the time by Λ / U_∞. The non-dimensional unsteady pressure p is introduced by writing the dimensional pressure as $(p_\infty + \rho_\infty U_\infty^2 p)$, where p_∞ is a constant.

The turbulent vorticity fluctuations in the free-stream are assumed to be of low intensity so that they can be treated as a linear perturbation about the mean flow. Mathematically, they can be represented as a superposition of sinusoidal disturbances:

$$\boldsymbol{u} - \hat{\boldsymbol{i}} = \epsilon \boldsymbol{u}_\infty(x - t, y, z) = \epsilon \hat{\boldsymbol{u}}^\infty \exp(\mathrm{i}(\boldsymbol{k} \cdot \boldsymbol{x} - k_1 t)) + \text{c.c.}, \tag{2.1}$$

where $\hat{\boldsymbol{u}}^\infty = \{\hat{u}_1^\infty, \hat{u}_2^\infty, \hat{u}_3^\infty\}$ with $\hat{u}_{1,2,3}^\infty = O(1)$, $\boldsymbol{k} = \{k_1, k_2, k_3\}$ are real vectors, and ϵ is a measure of the turbulence intensity. It follows from the continuity equation that

$$\hat{\boldsymbol{u}}^\infty \cdot \boldsymbol{k} = 0. \tag{2.2}$$

We focus on low-frequency (i.e. long-wavelength) components with $k_1 \ll 1$ since these are the ones that can penetrate into the boundary layer to form streaks. The linear nature of the problem allows us to calculate the signature of each Fourier component within the boundary layer; the overall effect of a free-stream turbulent flow with a continuous spectrum can be computed by a proper summation of the Fourier modes (§6).

Following LWG, a turbulent Reynolds number,

$$r_t = \epsilon R_\Lambda = O(1),$$

is defined, where

$$R_\Lambda \equiv U_\infty \Lambda / \nu_\infty,$$

and ν_∞ is the kinematic viscosity of air in the free stream. We take R_Λ to be asymptotically large, i.e. $R_\Lambda \gg 1$. It has been shown by Goldstein (1997) that, as $\epsilon \to 0$ while r_t is kept at $O(1)$, the flow domain can be divided into four well-defined asymptotic regions (figure 1). A brief description of the regions is given as follows.

Region I. This region has $O(\Lambda)$ dimensions in all three directions and accommodates the inviscid flow approaching the leading edge of the plate. The disturbances herein are treated as small perturbations of the oncoming uniform flow.

Region II. This is a viscous region underneath region I. The unsteady perturbations are governed by the linearized unsteady boundary-layer equations (LUBL); see Gulyaev *et al.* (1989) and LWG for the incompressible case.

The solution in this region is no longer valid when the boundary-layer thickness δ^* becomes comparable with Λ because the diffusion in the spanwise direction is then of the same order of that in the wall-normal direction. Since $\delta^* = O((\nu_\infty x^*/U_\infty)^{1/2})$ at a location x^*, setting $\delta^* = O(\Lambda)$ shows that the boundary-layer approximation becomes invalid at a downstream location where $x^* = O(\Lambda R_\Lambda)$, i.e. where

$$x/R_\Lambda = O(1).$$

Region III. This is a viscous region located at $O(\Lambda R_\Lambda)$ from the leading edge and has an $O(\Lambda)$ width. The disturbances are governed by the unsteady boundary-region equations (Kemp 1951), which are obtained from the full Navier–Stokes equations by neglecting the streamwise pressure-gradient and the streamwise viscous diffusion. Similarly to the boundary-layer equations, these equations are parabolic in the streamwise direction, but elliptic in the spanwise direction. Numerical solutions of these equations reveal that the response attains its maximum where $x = O(k_1^{-1})$. It follows that a distinguished scaling (in the sense that crossflow ellipticity is significant at the location where the disturbances are dominant) is

$$k_1 = O(R_\Lambda^{-1}). \tag{2.3}$$

Because of the disparity between the spanwise and streamwise scales, $O(\epsilon)$ fluctuations in the free stream can generate $O(\epsilon/k_1)$ streamwise velocity disturbances within the boundary layer (LWG). On noting (2.3), the condition for linearization, $\epsilon/k_1 \ll 1$, becomes

$$\epsilon R_\Lambda = r_t \ll 1. \tag{2.4}$$

This is the assumption that we shall make in the rest of the paper. The unsteady flow is then governed by linearized unsteady boundary-region equations.

Region IV. This is an outer region just above region III. The flow is influenced at leading order by the displacement effect due to the increased thickness of the viscous layer underneath. This implies that the solution takes different forms depending on whether the flow is subsonic, transonic or supersonic. FST in region IV should generally be regarded as nonlinear. However, as argued by LWG, the linearized equations hold over an interval of streamwise distances $x_L \ll 1/\epsilon = R_\Lambda/r_t$. In addition, viscous attenuation is negligible over a length much shorter than $O(R_\Lambda)$. If stationary and homogeneous turbulence $\epsilon \boldsymbol{u}_\infty$ is imposed at a distance $-x_L^\dagger$ upstream of the leading edge, with $x_L^\dagger$ satisfying

$$1 \ll -x_L^\dagger \ll R_\Lambda,$$

then locally the oncoming FST behaves like convected gusts, and can be specified independently of the mean flow (see (2.1)). Viscous attenuation has, however, to be taken into account in region IV, which covers an $O(R_\Lambda)$ streamwise distance.

3. The linear inviscid flow and the boundary-layer flow: regions I and II

The compressible inviscid flow of region I is analogous to the incompressible flow described by LWG. The analysis, the details of which given in Ricco (2006), shows that the velocities in the streamwise and spanwise directions at the wall are given by

$$\boldsymbol{u}(0) = \hat{\boldsymbol{\imath}} + \cdots + \epsilon \boldsymbol{u}^{(1)}(0)\exp(\mathrm{i}k_1(x-t) + \mathrm{i}k_3 z) + \text{c.c.},$$

where

$$u_\sigma^{(1)}(0) = \hat{u}_\sigma^\infty + \frac{\mathrm{i}k_\sigma}{\Gamma}\hat{u}_2^\infty \quad \text{for}\, \sigma = 1, 3, \quad u_2^{(1)}(0) = 0 \quad \text{with} \quad \Gamma = \left(k_1^2 + k_3^2\right)^{1/2}. \tag{3.1}$$

The streamwise and spanwise slip velocities, $u_1^{(1)}(0)$ and $u_3^{(1)}(0)$, are reduced to zero across the viscous region II, where the unsteady perturbation is superposed on a steady laminar compressible boundary layer. The latter is considered first.

3.1. *The steady compressible laminar boundary-layer flow*

The steady compressible equations are cast into a more compact form by means of the Dorodnitsyn–Howarth coordinate transformation (Stewartson 1964; Schlichting & Gersten 2000):

$$\overline{Y} = \overline{Y}(x, y) \equiv \int_0^y \rho(x, \check{y})\, \mathrm{d}\check{y}. \tag{3.2}$$

In the absence of pressure gradient, a similarity solution exists with the similarity variable defined as

$$\eta \equiv \overline{Y}\left(\frac{R_\Lambda}{2x}\right)^{1/2}. \tag{3.3}$$

The solution for the velocity and temperature can be expressed as

$$U = F'(\eta), \quad V = (2xR_\Lambda)^{-1/2}\left(-TF + \eta_c TF'\right), \quad T = T(\eta)$$

where a prime indicates differentiation with respect to η, and

$$\eta_c \equiv \frac{1}{T}\int_0^\eta T(\check{\eta})\, \mathrm{d}\check{\eta}.$$

It follows from the x-momentum and energy equations that F and T are governed by the coupled equations

$$\left[(\mu/T)F''\right]' + FF'' = 0, \tag{3.4}$$

$$Pr^{-1}\left[(\mu/T)T'\right]' + FT' + (\gamma-1)M^2(\mu/T)F''^2 = 0. \tag{3.5}$$

The boundary conditions are

$$F(0) = F'(0) = 0, \quad T'(0) = 0; \quad F' \to 1, \quad T \to 1 \ \text{ as } \ \eta \to \infty.$$

In (3.5), Pr is the Prandtl number (and is set to be 0.7 in our calculations). The variation of the viscosity with the temperature is assumed to obey the power law (Cebeci 2002),

$$\mu = T^{\omega} \quad \text{with} \quad \omega = 0.76.$$

This relation is preferred to the simpler Chapman law ($\omega = 1$) as it is a better model in the Mach-number range $M < 4$ (Stewartson 1964), which is of interest in this study.

3.2. *The unsteady velocity and temperature perturbation*

For a single Fourier component of the disturbance, the solution in the boundary layer can be expressed as:

$$\begin{aligned}\{u, v, w, \tau\} &= \{U, V, 0, T\}\\ &\quad + \epsilon\left\{\bar{u}_0(\bar{x},\eta), \left(\frac{2\bar{x}k_1}{R_\Lambda}\right)^{1/2}\bar{v}_0(\bar{x},\eta), \bar{w}_0(\bar{x},\eta), \bar{\tau}_0(\bar{x},\eta)\right\}\\ &\quad \times \exp(\mathrm{i}(k_3 z - k_1 t)) + \text{c.c.},\end{aligned} \tag{3.6}$$

where $\bar{x} = k_1 x$ is a scaled streamwise variable. Following LWG and Gulyaev *et al.* (1989), the solution is expressed as a sum of a 'two-dimensional' part and a three-dimensional part, namely

$$\left.\begin{aligned}\{\bar{u}_0, \bar{v}_0, \bar{\tau}_0\} &= \left(\hat{u}_1^{\infty} + \tfrac{\mathrm{i}k_1}{\Gamma}\hat{u}_2^{\infty}\right)\{\bar{u}^{(0)}, \bar{v}^{(0)}, \bar{\tau}^{(0)}\} + \tfrac{\mathrm{i}k_3}{k_1}\left(\hat{u}_3^{\infty} + \tfrac{\mathrm{i}k_3}{\Gamma}\hat{u}_2^{\infty}\right)\{\bar{u}, \bar{v}, \bar{\tau}\},\\ \bar{w}_0 &= \left(\hat{u}_3^{\infty} + \tfrac{\mathrm{i}k_3}{\Gamma}\hat{u}_2^{\infty}\right)\bar{w}.\end{aligned}\right\} \tag{3.7}$$

The 'two-dimensional' part $\{\bar{u}^{(0)}, \bar{v}^{(0)}, 0, \bar{\tau}^{(0)}\}$ is driven directly by the streamwise slip velocity. Obviously, this part of the signature is smaller than the three-dimensional part by a factor $k_1/k_3 \ll 1$, and hence will not be considered any further. The three-dimensional part $\{\bar{u}, \bar{v}, \bar{w}, \bar{\tau}\}$ satisfies the LUBL equations, which read:

Continuity equation

$$\frac{\partial \bar{u}}{\partial \bar{x}} + \frac{\eta_c}{2\bar{x}}\left(\frac{T'}{T}\bar{u} - \frac{\partial \bar{u}}{\partial \eta}\right) - \frac{T'}{T^2}\bar{v} + \frac{1}{T}\frac{\partial \bar{v}}{\partial \eta} + \bar{w} + \left(\frac{\mathrm{i}}{T} - \frac{FT'}{2\bar{x}T^2}\right)\bar{\tau} - \frac{F'}{T}\frac{\partial \bar{\tau}}{\partial \bar{x}} + \frac{F}{2\bar{x}T}\frac{\partial \bar{\tau}}{\partial \eta} = 0, \tag{3.8}$$

x-Momentum equation

$$\begin{aligned}-\left(\mathrm{i} + \frac{\eta_c F''}{2\bar{x}}\right)\bar{u} + F'\frac{\partial \bar{u}}{\partial \bar{x}} - \frac{1}{2\bar{x}}\left(F + \frac{\mu' T'}{T} - \frac{\mu T'}{T^2}\right)\frac{\partial \bar{u}}{\partial \eta} - \frac{\mu}{2\bar{x}T}\frac{\partial^2 \bar{u}}{\partial \eta^2} + \frac{F''}{T}\bar{v}\\ + \left(\frac{FF'' - \mu'' T' F'' - \mu' F'''}{2\bar{x}T} + \frac{\mu' F'' T'}{2\bar{x}T^2}\right)\bar{\tau} - \frac{\mu' F''}{2\bar{x}T}\frac{\partial \bar{\tau}}{\partial \eta} = 0,\end{aligned} \tag{3.9}$$

z-Momentum equation

$$-\mathrm{i}\bar{w} + F'\frac{\partial \bar{w}}{\partial \bar{x}} - \frac{1}{2\bar{x}}\left(F + \frac{\mu' T'}{T} - \frac{\mu T'}{T^2}\right)\frac{\partial \bar{w}}{\partial \eta} - \frac{\mu}{2\bar{x}T}\frac{\partial^2 \bar{w}}{\partial \eta^2} = 0, \tag{3.10}$$

Energy equation

$$-\frac{\eta_c T'}{2\bar{x}}\bar{u}-\frac{M^2(\gamma-1)\mu F''}{\bar{x}T}\frac{\partial \bar{u}}{\partial \eta}+\frac{T'}{T}\bar{v}-\left[\mathrm{i}-\frac{FT'}{2\bar{x}T}+\frac{1}{2Pr\bar{x}}\left(\frac{\mu' T'}{T}\right)'+\frac{M^2(\gamma-1)\mu' F''^2}{2\bar{x}T}\right]\bar{\tau}$$

$$+F'\frac{\partial \bar{\tau}}{\partial \bar{x}}-\frac{1}{2\bar{x}}\left(F+\frac{2\mu' T'}{PrT}-\frac{\mu T'}{PrT^2}\right)\frac{\partial \bar{\tau}}{\partial \eta}-\frac{\mu}{2Pr\bar{x}T}\frac{\partial^2 \bar{\tau}}{\partial \eta^2}=0, \qquad (3.11)$$

where $\mu' = \mathrm{d}\mu/\mathrm{d}T$. Equations (3.8)–(3.11) satisfy the boundary conditions

$$\bar{u}=\bar{v}=\bar{w}=\bar{\tau}=0 \ \text{ at } \ \eta=0, \quad \bar{\tau}\rightarrow 0 \ \text{ as } \ \eta\rightarrow\infty.$$

Matching with the inviscid free-stream solution implies that

$$\bar{u}\rightarrow 0, \ \bar{w}\rightarrow \mathrm{e}^{\mathrm{i}\bar{x}}, \ \bar{\tau}\rightarrow 0 \ \text{ as } \ \eta\rightarrow\infty.$$

Note that $\mathrm{e}^{\mathrm{i}\bar{x}}$ is the only forcing term, implying that the spanwise component of the free-stream fluctuation is the sole driving factor at leading order for the formation of streaks inside the boundary layer.

In order to solve the parabolic system (3.8)–(3.11) by a marching procedure, upstream three-dimensional velocity and temperature profiles must be specified. These can be derived by considering the limit $\bar{x} \ll 1$, for which the solution expands as

$$\{\bar{u},\bar{v},\bar{w},\bar{\tau}\}=\{\bar{x}U_I, V_I, W_I, \bar{x}T_I\}+\mathrm{i}\bar{x}\{\bar{x}U_{II}, V_{II}, W_{II}, \bar{x}T_{II}\}+\cdots . \qquad (3.12)$$

Substituting these into equations (3.8)–(3.11), and collecting terms of $O(1)$ and $O(\bar{x})$, we obtain the systems of ordinary differential equations for the first two terms $\{U_j, V_j, W_j, T_j\}$ $(j = I,\ II)$. These equations and solutions are given in Ricco (2006).

3.3. *Unsteady boundary-layer solution*

The LUBL equations (3.8)–(3.11) are solved by a second-order Keller-box finite-difference method (Cebeci 2002) to march in the downstream direction, starting from the two-term approximation for the initial profiles (3.12). For a compressible boundary layer, the velocity and temperature fluctuations are coupled. As a result, external disturbances of the hydrodynamic kind (i.e. the convected gust) trigger thermal disturbance $\bar{\tau}$ inside the boundary layer. Figure 2 shows the profiles of the (streamwise and spanwise) velocity and temperature fluctuations for $M = 3$. The temperature profile is similar to that of the streamwise velocity and evolves in a similar manner. The perturbations initially concentrate in the core of the boundary layer, but eventually move upward towards the free stream. They finally concentrate in an edge layer located at the outer reach of the boundary layer, whereas their signature in the main bulk is exponentially small. The asymptotic solution for $\bar{x} \gg 1$ was constructed by LWG for the incompressible case and was generalized to include compressibility by Ricco (2006).

Taylor (1939) and Klebanoff (1971) argued that streaks could originate from a spanwise-alternating thickening and thinning of the boundary layer. The same result was found by Crow (1966) in his study of the response of a laminar boundary layer to small steady spanwise periodic perturbations in the free stream. Mathematically, the argument is that the streamwise velocity of the perturbed flow is represented by $F'(y/(\delta_0+\delta_1))$, where δ_0 denotes the unperturbed thickness and $\delta_1 = \delta_1(z)$ the variation of the thickness. A simple Taylor expansion for small δ_1 shows that the streak profile is approximated by $\eta F''$. In the incompressible case, this result agrees with the small-$\bar{x}$ asymptotic limit of the boundary-layer solution derived by LWG,

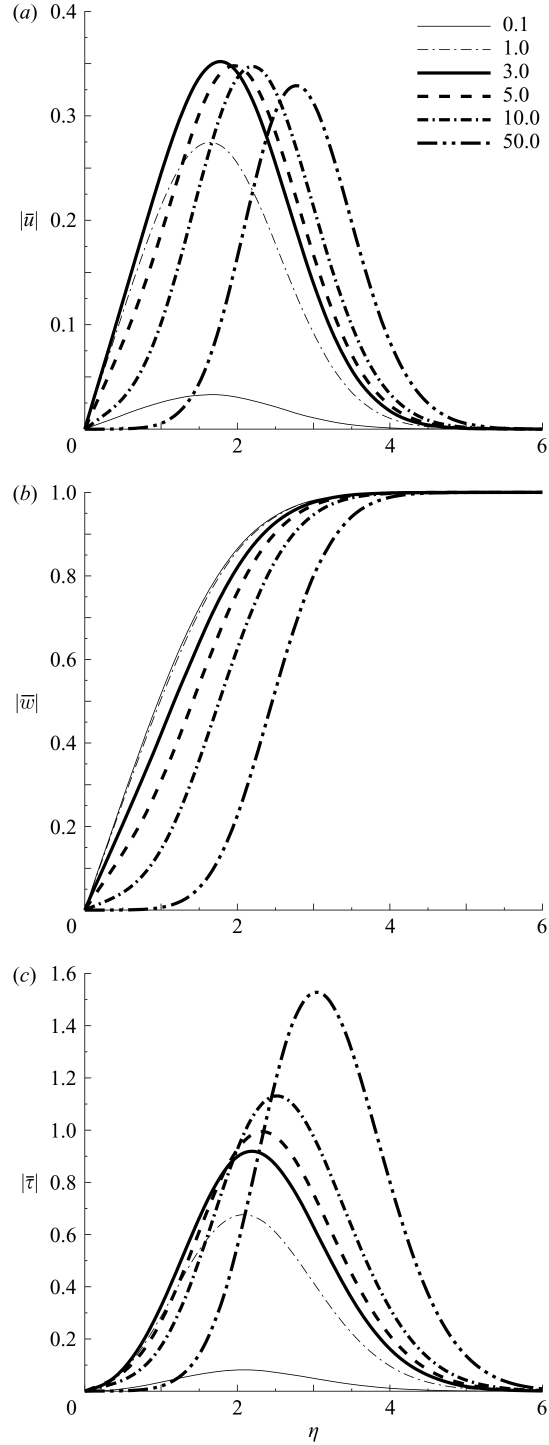

FIGURE 2. Downstream evolution of the fluctuation profiles for $M = 3$. (*a*) Streamwise velocity ($\bar{u}$); (*b*) spanwise velocity ($\bar{w}$); (*c*) temperature ($\bar{\tau}$). The numbers in the figure indicate the values of $\bar{x}$.

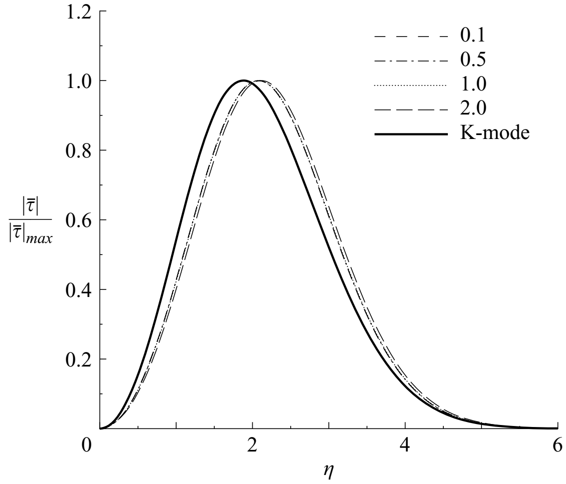

FIGURE 3. Profiles of scaled temperature profiles at different $\bar{x}$ locations at $M = 3$ and comparison with $\eta T'/(\eta T')_{max}$ (labelled as K-mode).

namely $\bar{u} \rightarrow (1/2)\bar{x}\eta F''$. The same physical argument applied to the temperature fluctuation would give a profile $\eta T'$. Unfortunately, for a compressible boundary layer these expressions fail to satisfy the governing equations, which implies that Taylor's argument cannot be carried over. In figure 3, we compare the temperature perturbation profiles at small $\bar{x}$ locations for $M = 3$ with $\eta T'$. The boundary-layer solution for $\bar{x} < 2$ is similar to the shape $\eta T'$, although the latter is slightly skewed toward small η values. It must be noted that even in the incompressible limit, the prediction based on the argument of alternating boundary-layer thicknesses is correct only for relatively small $\bar{x}$. The entire evolution of velocity and temperature fluctuations can only be predicted by the appropriate matching with the free-stream continuous forcing.

The numerical results indicate that in the region where $\eta = O(1)$, both the streamwise velocity and temperature reach their maximum values at $\bar{x} = O(1)$, i.e. $x \sim k_1^{-1}$. This means that long-wavelength (low-frequency) components in the FST survive at a downstream distance comparable with their streamwise length scale. The resulting velocity and temperature fields exhibit elongated streaky structures in the x-direction, which modulate slowly in time. These are the predominant signatures since their physical magnitudes are given by $\bar{u}$ and $\bar{\tau}$ multiplied by a factor $O(k_3/k_1)$; see (3.7).

4. The boundary-region flow (region III) and the inviscid outer solution (region IV)

The boundary-layer equations are valid only in the region sufficiently upstream where the boundary-layer thickness δ^* is much smaller than Λ. As was explained in §2, δ^* eventually becomes comparable with Λ when $x/R_\Lambda = O(1)$. The boundary-region equations then have to be employed in order to describe the viscous motion in region III. Experimental evidence in the incompressible case (e.g. Kendall 1985; Westin *et al.* 1994) suggests that, when streaky structures are well developed, their spanwise wavelength is more-or-less $O(\delta^*)$. We expect this to be the case in compressible boundary layers because in both the compressible and incompressible regimes, streaks amplify up to the location where $\delta^* \sim \Lambda$, after which they start to decay. The opposite limit $\delta^* \gg \Lambda$ is of little interest since streaks would have decayed to a negligible amplitude.

The unsteady displacement induced by the viscous motion within the boundary-layer now influences the inviscid flow in region IV to generate an unsteady pressure. The latter appears as a new unknown. Hence, the y-momentum equation must also be considered. Similarly to the velocity and temperature, the unsteady pressure is expressed as a sum of 'two-dimensional' and three-dimensional components, namely

$$p = \epsilon \left[\frac{k_1}{R_\Lambda} \left(\hat{u}_1^\infty + \frac{\mathrm{i}k_1}{\Gamma} \hat{u}_2^\infty \right) \overline{p}^{(0)} + \mathrm{i}\kappa \left(\frac{k_1}{R_\Lambda} \right)^{1/2} \left(\hat{u}_3^\infty + \frac{\mathrm{i}k_3}{\Gamma} \hat{u}_2^\infty \right) \overline{p} \right] \exp(\mathrm{i}(k_3 z - k_1 t)) + \text{c.c.}$$

The latter part of the disturbance, $\{\overline{u}, \overline{v}, \overline{w}, \overline{\tau}, \overline{p}\}$, is again dominant because $k_1/R_\Lambda \ll \kappa(k_1/R_\Lambda)^{1/2}$. Only this part will be considered hereinafter, and it is governed by the boundary-region equations, which read

Continuity equation

$$\frac{\partial \overline{u}}{\partial \overline{x}} + \frac{\eta_c}{2\overline{x}} \left(\frac{T'}{T} \overline{u} - \frac{\partial \overline{u}}{\partial \eta} \right) - \frac{T'}{T^2} \overline{v} + \frac{1}{T} \frac{\partial \overline{v}}{\partial \eta} + \overline{w} + \left(\frac{\mathrm{i}}{T} - \frac{F T'}{2\overline{x} T^2} \right) \overline{\tau} - \frac{F'}{T} \frac{\partial \overline{\tau}}{\partial \overline{x}} + \frac{F}{2\overline{x} T} \frac{\partial \overline{\tau}}{\partial \eta} = 0, \tag{4.1}$$

x-Momentum equation

$$\begin{aligned} &\left(-\mathrm{i} - \frac{\eta_c F''}{2\overline{x}} + \mu\kappa^2 T \right) \overline{u} + F' \frac{\partial \overline{u}}{\partial \overline{x}} - \frac{1}{2\overline{x}} \left(F + \frac{\mu' T'}{T} - \frac{\mu T'}{T^2} \right) \frac{\partial \overline{u}}{\partial \eta} - \frac{\mu}{2\overline{x} T} \frac{\partial^2 \overline{u}}{\partial \eta^2} + \frac{F''}{T} \overline{v} \\ &\quad + \left(\frac{F F'' - \mu'' T' F'' - \mu' F'''}{2\overline{x} T} + \frac{\mu' F'' T'}{2\overline{x} T^2} \right) \overline{\tau} - \frac{\mu' F''}{2\overline{x} T} \frac{\partial \overline{\tau}}{\partial \eta} = 0, \end{aligned} \tag{4.2}$$

y-Momentum equation

$$\begin{aligned} &\frac{1}{4\overline{x}^2} \left[F T + \eta_c (F T' - T F') - \eta_c^2 F'' T \right] \overline{u} \\ &\quad + \frac{\mu' T'}{3\overline{x}} \frac{\partial \overline{u}}{\partial \overline{x}} - \frac{\mu}{6\overline{x}} \frac{\partial^2 \overline{u}}{\partial \eta \partial \overline{x}} + \frac{1}{12\overline{x}^2} \left[\mu + \eta_c T \left(\frac{\mu}{T} \right)' \right] \frac{\partial \overline{u}}{\partial \overline{\eta}} \\ &\quad + \frac{\eta_c \mu}{12\overline{x}^2} \frac{\partial^2 \overline{u}}{\partial \eta^2} + \left(-\mathrm{i} + \mu\kappa^2 T + \frac{F'}{2\overline{x}} + \frac{\eta_c F''}{2\overline{x}} - \frac{F T'}{2\overline{x} T} \right) \overline{v} + F' \frac{\partial \overline{v}}{\partial \overline{x}} \\ &\quad - \frac{1}{\overline{x}} \left(\frac{F}{2} + \frac{2\mu' T'}{3T} - \frac{2\mu T'}{3T^2} \right) \frac{\partial \overline{v}}{\partial \eta} - \frac{2\mu}{3\overline{x} T} \frac{\partial^2 \overline{v}}{\partial \eta^2} + \frac{\mu' T'}{3\overline{x}} \overline{w} - \frac{\mu}{6\overline{x}} \frac{\partial \overline{w}}{\partial \eta} + \frac{1}{2\overline{x}} \frac{\partial \overline{p}}{\partial \eta} \\ &\quad + \frac{1}{4\overline{x}^2} \left\{ \eta_c \left[(F F')' - T \left(\frac{\mu' F''}{T} \right)' \right] - F F' - \frac{F^2 T'}{T} - \mu' F'' + \frac{4}{3} \left(\frac{\mu' T' F}{T} \right)' \right\} \overline{\tau} \\ &\quad - \frac{\mu' F''}{2\overline{x}} \frac{\partial \overline{\tau}}{\partial \overline{x}} - \left(\frac{\eta_c \mu' F''}{4\overline{x}^2} - \frac{\mu' T' F}{3\overline{x}^2 T} \right) \frac{\partial \overline{\tau}}{\partial \eta} = 0, \end{aligned} \tag{4.3}$$

z-Momentum equation

$$\begin{aligned} &-\frac{\eta_c \mu' T' T \kappa^2}{2\overline{x}} \overline{u} + \frac{\mu T \kappa^2}{3} \frac{\partial \overline{u}}{\partial \overline{x}} - \frac{\eta_c \mu T \kappa^2}{6\overline{x}} \frac{\partial \overline{u}}{\partial \eta} + \mu' T' \kappa^2 \overline{v} + \frac{\mu\kappa^2}{3} \frac{\partial \overline{v}}{\partial \eta} - \left(\mathrm{i} - \frac{4\mu T \kappa^2}{3} \right) \overline{w} \\ &\quad + F' \frac{\partial \overline{w}}{\partial \overline{x}} - \frac{1}{2\overline{x}} \left(F + \frac{\mu' T'}{T} - \frac{\mu T'}{T^2} \right) \frac{\partial \overline{w}}{\partial \eta} - \frac{\mu}{2\overline{x} T} \frac{\partial^2 \overline{w}}{\partial \eta^2} + \frac{\mu' F T' \kappa^2}{3\overline{x}} \overline{\tau} - \kappa^2 T \overline{p} = 0, \end{aligned} \tag{4.4}$$

Energy equation

$$-\frac{\eta_c T'}{2\overline{x}}\overline{u}-\frac{M^2(\gamma-1)\mu F''}{\overline{x}T}\frac{\partial\overline{u}}{\partial\eta}+\frac{T'}{T}\overline{v}+\left[-\mathrm{i}+\frac{FT'}{2\overline{x}T}-\frac{1}{2Pr\overline{x}}\left(\frac{\mu'T'}{T}\right)'-\frac{M^2(\gamma-1)\mu'F''^2}{2\overline{x}T}\right.$$

$$\left.+\frac{\mu\kappa^2T}{Pr}\right]\overline{\tau}+F'\frac{\partial\overline{\tau}}{\partial\overline{x}}-\frac{1}{2\overline{x}}\left(F+\frac{2\mu'T'}{PrT}-\frac{\mu T'}{PrT^2}\right)\frac{\partial\overline{\tau}}{\partial\eta}-\frac{\mu}{2Pr\overline{x}T}\frac{\partial^2\overline{\tau}}{\partial\eta^2}=0, \qquad (4.5)$$

where we have put

$$\kappa\equiv k_3/(k_1R_\Lambda)^{1/2}=O(1). \qquad (4.6)$$

Note that the pressure appears only in the y- and z-momentum equations. The streamwise pressure gradient in the x-momentum equation and the term representing the work done by the pressure in the energy equation are both negligible.

4.1. *Large-η boundary conditions*

The analysis to obtain the outer (or far-field) boundary conditions for (4.1)–(4.5) is analogous to LWG and can be found in Ricco (2006). The resulting boundary conditions are of the mixed type, namely as $\eta\to\infty$

$$\overline{u}\to 0,\quad \overline{\tau}\to 0, \qquad (4.7)$$

$$\frac{\partial\overline{v}}{\partial\eta}+|\kappa|(2\overline{x})^{1/2}\overline{v}\to-\exp(\mathrm{i}(\overline{x}+\kappa_2(2\overline{x})^{1/2}\overline{\eta}))\exp\left(-\left(\kappa^2+\kappa_2^2\right)\overline{x}\right), \qquad (4.8)$$

$$\frac{\partial\overline{w}}{\partial\eta}+|\kappa|(2\overline{x})^{1/2}\overline{w}\to\mathrm{i}\kappa_2(2\overline{x})^{1/2}\exp\left(\mathrm{i}(\overline{x}+\kappa_2(2\overline{x})^{1/2}\overline{\eta})\right)\exp(-(\kappa^2+\kappa_2^2)\overline{x}), \qquad (4.9)$$

$$\frac{\partial\overline{p}}{\partial\eta}+|\kappa|(2\overline{x})^{1/2}\overline{p}\to 0, \qquad (4.10)$$

where $\overline{\eta}\equiv\eta-\beta_c$, $\beta_c=\lim_{\eta\to\infty}(\eta-F)$ and $\kappa_2\equiv k_2/(k_1R_\Lambda)^{1/2}=O(1)$. The compressible effect has been distilled into β_c. The non-zero terms on the right-hand sides of (4.8) and (4.9) represent the forcing of the external vortical disturbances on the viscous layer.

4.2. *Upstream behaviour of the boundary-region solution*

In order to specify the appropriate initial condition for the boundary-region equations, we first seek the power series solution for $\eta=O(1)$ and $\overline{x}\ll O(1)$,

$$\{\overline{u},\overline{v},\overline{w},\overline{\tau},\overline{p}\}=\sum_{n=0}^{\infty}(2\overline{x})^{n/2}\left\{2\overline{x}U_n(\eta),\,V_n(\eta),\,W_n(\eta),\,2\overline{x}T_n(\eta),\,P_n(\eta)/(2\overline{x})^{1/2}\right\}. \qquad (4.11)$$

Substituting (4.11) into (4.1)–(4.5) and collecting like powers of $\overline{x}$, we obtain a system of ordinary differential equations. The equations governing the first two terms, which are required in order to start the marching procedure, are given in Appendix D in Ricco (2006). The upstream conditions for the boundary-region equations are obtained by constructing a composite solution that is uniformly valid for all values of η (see Ricco 2006, §2.4.2.). This yields the initial condition to be imposed for $\overline{x}\ll 1$,

$$\overline{u}\to 2\overline{x}U_0+(2\overline{x})^{3/2}U_1, \qquad (4.12)$$

$$\overline{v}\to V_0+(2\overline{x})^{1/2}V_1+\frac{\mathrm{i}}{(\kappa_2-\mathrm{i}|\kappa|)(2\overline{x})^{1/2}}\left(\exp\left(\mathrm{i}\kappa_2(2\overline{x})^{1/2}\overline{\eta}-\left(\kappa^2+\kappa_2^2\right)\overline{x}\right)\right.$$

$$\left.-\exp(-|\kappa|(2\overline{x})^{1/2}\overline{\eta})\right)-\left(V_c-\tfrac{1}{2}g_1|\kappa|(2\overline{x})^{1/2}\right)\exp(-|\kappa|(2\overline{x})^{1/2}\overline{\eta})-\overline{v}_c, \qquad (4.13)$$

$$\overline{w} \to W_0 + (2\overline{x})^{1/2} W_1 + \frac{1}{\kappa_2 - \mathrm{i}|\kappa|} \left(\kappa_2 \exp\left(\mathrm{i}\kappa_2 (2\overline{x})^{1/2} \overline{\eta} - \left(\kappa^2 + \kappa_2^2 \right) \overline{x} \right) \right.$$

$$\left. - \mathrm{i}|\kappa| \exp(-|\kappa| (2\overline{x})^{1/2} \overline{\eta}) \right) - V_c |\kappa| (2\overline{x})^{1/2} \exp(-|\kappa| (2\overline{x})^{1/2} \overline{\eta}) - \overline{w}_c, \tag{4.14}$$

$$\overline{\tau} \to 2\overline{x} T_0 + (2\overline{x})^{3/2} T_1, \tag{4.15}$$

$$\overline{p} \to \frac{P_0}{(2\overline{x})^{1/2}} + P_1 + \left(g_1 - \frac{V_c}{|\kappa| (2\overline{x})^{1/2}} \right) \exp(-|\kappa| (2\overline{x})^{1/2} \overline{\eta}) - \overline{p}_c, \tag{4.16}$$

where V_c, g_1 and the common parts $\overline{v}_c$, $\overline{w}_c$ and $\overline{p}_c$ are given in Appendix D in Ricco (2006).

The system (4.1)–(4.5) is solved by a second-order finite-difference scheme which is central in η and backward in $\overline{x}$. The outer boundary conditions (4.7)–(4.10) are applied by a second-order finite-difference discretization scheme. The pressure is computed on a grid staggered in the η-direction with respect to that for the velocity in order to avoid the pressure decoupling phenomenon. The pressure at the wall then need not be specified; its value is calculated *a posteriori* by setting $\eta = 0$ in the z-momentum equation.

4.3. *Boundary-region solutions*

The numerical results for the case of a free-stream disturbance consisting of a single Fourier component are first presented. As a check of our code, we shall verify that the boundary-region solution matches the boundary-layer solution in the two limits: (*a*) as $\kappa, \kappa_2 \to 0$ for fixed $\overline{x}$ and (*b*) as $\overline{x} \to 0$ for fixed κ and κ_2. LWG have already demonstrated this in the incompressible case. We repeated their calculations and were able to reproduce their result (see Ricco 2006). The result for $M = 2$ is shown in figure 4, where the downstream evolution of the maximum streamwise velocity, $|\overline{u}|_{max} = \max_\eta |\overline{u}|$, computed from the boundary-region equations, is compared with the boundary-layer solution (corresponding to $\kappa = -\kappa_2 = 0$). The downstream evolution of the maximum temperature fluctuation $|\overline{\tau}|_{max}$ is also shown. The boundary-region and boundary-layer solutions are quite different for the majority of $\overline{x}$ when κ and $\kappa_2 = O(1)$. When the value of $\kappa = -\kappa_2$ is reduced, the boundary-region solution approaches the boundary-layer solution as expected. The two become almost indistinguishable for $\kappa = -\kappa_2 < 0.005$. On the other hand, for fixed κ and κ_2, the boundary-region solution overlaps the boundary-layer solution for $\overline{x} \ll 1$. The overlapping region is, however, quite small for $\kappa = -\kappa_2 > 0.1$, indicating that the effect of crossflow ellipticity is already significant. This has a slightly stronger influence in the compressible case as the boundary-region solution deviates more from the boundary-layer solution than in the incompressible case at fixed values of κ and κ_2.

Figures 5 and 6 show the profiles of the streamwise and spanwise velocities at different streamwise positions for a Mach 3 boundary layer. The distributions resemble the $M = 0$ counterparts shown in LWG. Significant for the compressible case is that vortical disturbances generate substantial temperature fluctuations, the profiles of which are displayed in figure 7. At the same $\overline{x}$, the temperature and streamwise velocity profiles are similar. For the present case with $\kappa, \kappa_2 = O(1)$, the peak positions do not drift towards the free stream (cf. figure 2). Instead, the disturbance eventually attenuates across the entire boundary layer, indicating that the trapping of the response in the edge layer is a phenomenon only pertaining to disturbances with very small κ.

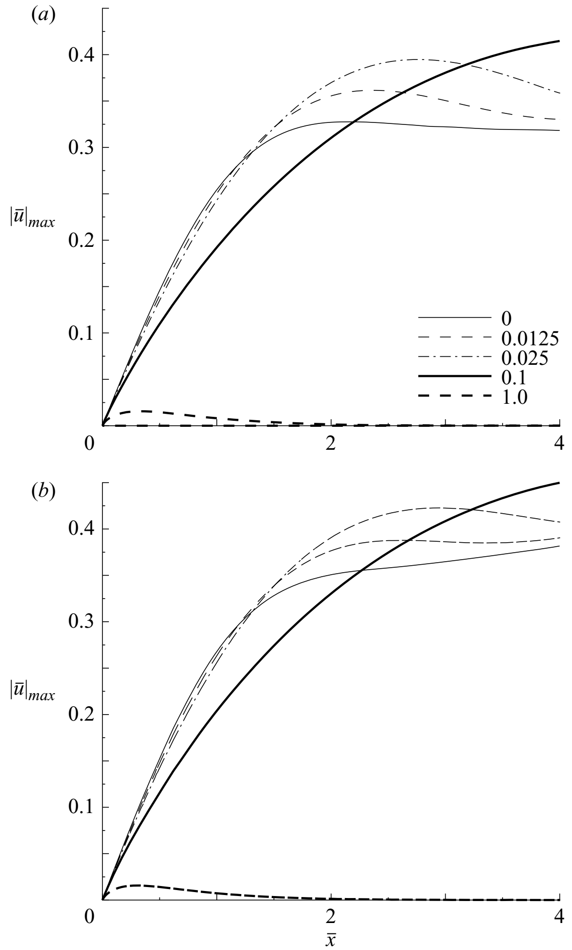

FIGURE 4. Comparison of the boundary-region solution with the boundary-layer solution ($\kappa = 0$) for $M = 2$. (*a*) Streamwise velocity; (*b*) temperature. The numbers in the graph indicate the values of $\kappa = -\kappa_2$.

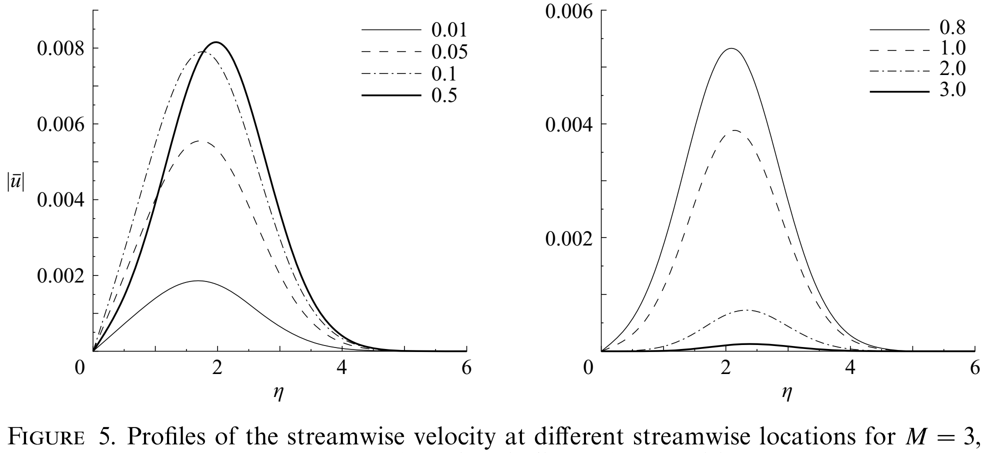

FIGURE 5. Profiles of the streamwise velocity at different streamwise locations for $M = 3$, $\kappa = -\kappa_2 = 1$. The values indicate the $\bar{x}$ position.

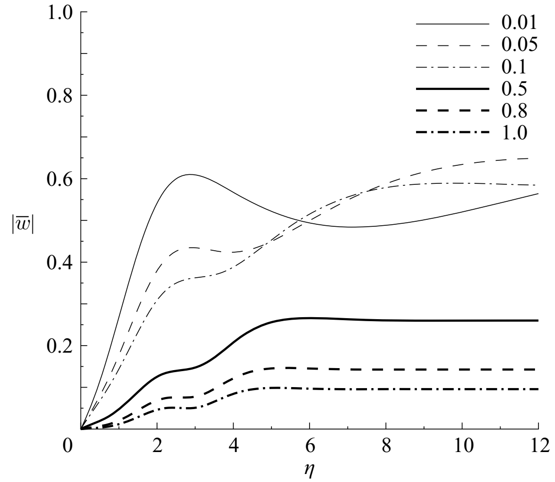

FIGURE 6. Profiles of the spanwise velocity for $M = 3$, $\kappa = -\kappa_2 = 1$. The values indicate the $\overline{x}$ position.

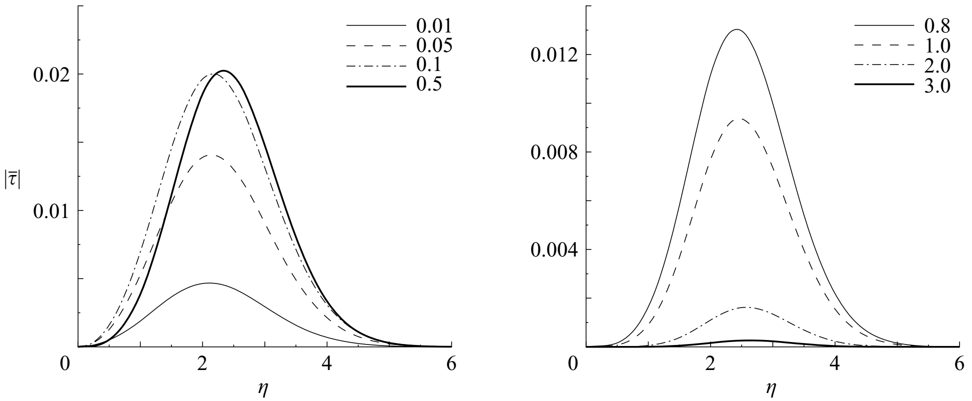

FIGURE 7. Profiles of the temperature for $M = 3$, $\kappa = -\kappa_2 = 1$. The values indicate the $\overline{x}$ position.

In addition to velocity and temperature fluctuations, we shall monitor the mass flux fluctuation $|\overline{\rho u}|$, since this is the quantity that is usually measured directly in experiments of compressible flows (e.g. Graziosi & Brown 2002). It is defined as

$$|\overline{\rho u}| = |(\rho + \overline{\rho})(U + \overline{u}) - \rho U| \approx |\rho \overline{u} + \overline{\rho} U| = \left| \frac{\overline{u}}{T} - \frac{U \overline{\tau}}{T^2} \right|$$

where ρ and $\overline{\rho}$ stand for the mean density and the density fluctuation, respectively. The nonlinear product is neglected, consistently with the adopted linearized approximation.

To examine the effect of compressibility, we consider $\{|u|, |\tau|, |\rho u|\}$, the velocity, temperature and mass flux fluctuations normalized by the intensity of the free-stream streamwise velocity component. They are related to $\{|\overline{u}|, |\overline{\tau}|, |\overline{\rho u}|\}$ via the relation

$$\{|u|, |\tau|, |\rho u|\} = \Upsilon \{|\overline{u}|, |\overline{\tau}|, |\overline{\rho u}|\}, \tag{4.17}$$

M	U_∞ (m s^{-1})	R_Λ	k_1	$\hat{u}_2^\infty$	$\hat{u}_3^\infty$	Υ
0.08	27.7	18 331.13	0.0453987	0.99639	−1.00360	195.72
0.7	242.2	160 397.35	0.0051884	0.99958	−1.00042	1712.61
2	692	458 278.15	0.0018160	0.99986	−1.00014	4893.18
4	1384	916 556.29	0.0009080	0.99994	−1.00006	9786.36

TABLE 1. Properties of convective gust with $f^* = 20$ Hz and $\kappa = \kappa_2 = 0.2178$.

M	U_∞ (m s^{-1})	R_Λ	k_1	$\hat{u}_2^\infty$	$\hat{u}_3^\infty$	Υ
2	692	458 278.14	0.0907974	0.99274	−1.00720	97.86
3	1038	687 417.22	0.0605316	0.99518	−1.00480	146.80
4	1384	916 556.29	0.0453987	0.99639	−1.00360	195.73

TABLE 2. Properties of convective gust with $f^* = 1$ kHz and $\kappa = \kappa_2 = 0.0308$.

where the normalization factor

$$\Upsilon = (k_3/k_1)\left[\left(\hat{u}_3^\infty\right)^2 + \left(k_3\hat{u}_2^\infty/\Gamma\right)^2\right]^{1/2}$$

is computed from (3.7). We assume that the variation of M is solely due to the change of U_∞, while the mean free-stream temperature is constant ($T_\infty = 298$ K and thus $c_\infty = 346$ m s^{-1}). The physical frequency f^* of the convective gust and its wavenumbers, $k_y^* = k_z^* = 2\pi/\Lambda$, are all fixed with $\Lambda = 0.01$ m. The streamwise wavenumber thus varies according to $k_x^* = 2\pi f^*/U_\infty$. The intensity of the gust, $Tu = \epsilon[(\hat{u}_1^\infty)^2 + (\hat{u}_2^\infty)^2 + (\hat{u}_3^\infty)^2]^{1/2}$, is kept constant ($Tu = \epsilon\sqrt{3}$), which means that the physical amplitude of the free-stream perturbation varies proportionally to U_∞. Without losing generality, we may set $\hat{u}_1^\infty = 1$, and $\hat{u}_2^\infty$ and $\hat{u}_3^\infty$ are determined from (2.2) and the condition of constant fluctuation intensity.

The influence of compressibility is illustrated for two cases, one with $f^* = 20$ Hz and the other with $f^* = 1000$ Hz, designated as case 1 and case 2, respectively. The parameters describing the mean flow and the free-stream perturbations are summarized in tables 1 and 2. Since k_1 decreases with U_∞, i.e. M, the 'low-frequency' band in the higher speed regime covers a broader range of physical frequencies. For instance, for $M > 2$, it may consist of components with dimensional frequencies up to 1 kHz (see table 2).

The results for case 1 are displayed in figure 8, where we plot the maxima of the streamwise velocity, temperature and mass flux against x for a range of M values. As M increases, both the temperature and mass-flux fluctuations become more intense. The streamwise velocity increases with M for M up to 2, but it decreases with M for $M > 2$.

Case 2 focuses on the supersonic regime, for which a disturbance of 1 kHz falls within the low-frequency band. The downstream development of the fluctuations for case 2 is shown in figure 9. Compressibility always enhances the temperature and mass-flux fluctuations, but, differently from case 1, the streamwise velocity also always increases with M. Overall, the fluctuations are stronger in case 1 than in case 2, confirming again that low-frequency disturbances are more readily entrained into the boundary layer.

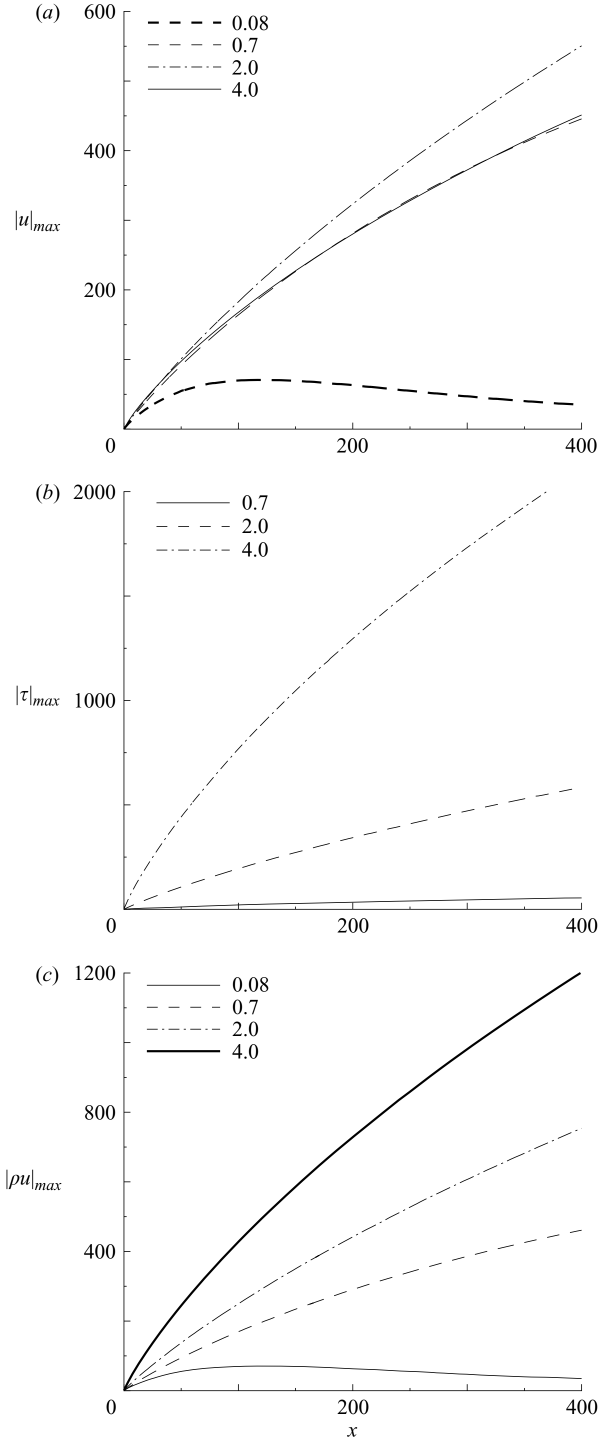

FIGURE 8. Boundary-region solutions for case 1 (table 1). (*a*) Streamwise velocity fluctuation; (*b*) temperature fluctuation; (*c*) mass flux fluctuation. The values indicate the Mach number.

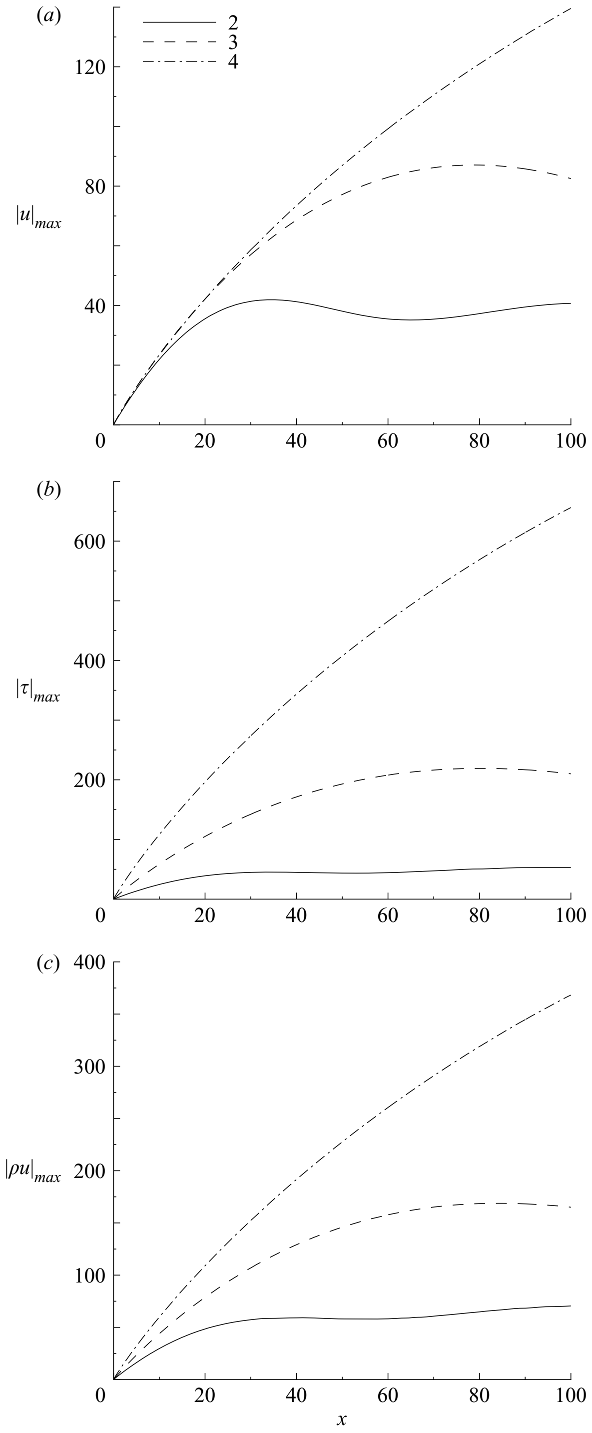

FIGURE 9. Boundary-region solutions for case 2 (table 2). (*a*) Streamwise velocity fluctuation; (*b*) temperature fluctuation; (*c*) mass flux fluctuation. The values indicate the Mach number.

$\bar{x}$	x^* (m)	$\epsilon\|u\|_{max}$ (%)	$\epsilon\|\tau\|_{max}$ (%)
0.10	0.033	5.90	14.84
0.25	0.082	11.94	30.22
0.50	0.165	19.53	49.73
4.5	1.482	51.97	131.83

TABLE 3. Maximum amplitudes of thermal and velocity streaks at different streamwise locations in a Mach 3 boundary layer. The gust intensity corresponds to $\epsilon = 1\%$. The last position $\bar{x} = 4.5$ is the downstream location where $\epsilon|\tau|_{max}$ (%) reaches its peak value. Other parameters are: $f^* = 300$ Hz, $\Lambda = 0.01$ m for which $R_\Lambda = 21\,695$, $k_1 = 0.0304$ and $\kappa = \kappa_2 = 0.245$.

In both cases, significant temperature fluctuation is induced even for a moderate Mach number, and thus 'thermal streaks' are expected to form. In order to provide a concrete estimate in physical terms, we present in table 3 the maximum amplitudes of the temperature and velocity streaks $\epsilon|\tau|_{max}$ (%) and $\epsilon|u|_{max}$ (%) induced in a Mach 3 boundary layer by a gust with intensity $\epsilon = 1\%$, $f^* = 300$ Hz and $\Lambda = 0.01$ m. At the downstream position $\bar{x} \approx 4.5$, $\epsilon|\tau|_{max}$ reaches its peak value of 132%. In the majority of the region upstream of the peak position, this amplitude is about 30–50%, while the corresponding velocity fluctuation is 10–20% of the mean free-stream velocity U_∞.

It thus seems likely that in practical situations, thermal streaks of considerable amplitude would arise. They could significantly affect the heat transfer. More importantly, they may fundamentally alter the secondary instability, that is, in the moderate Mach-number regime, both velocity and thermal streaks will have to be considered in the formulation of the secondary instability problem. This is in contrast with the incompressible case, where the streamwise velocity streaks are the principal quantity controlling the streak instability.

5. Receptivity: generation of highly oblique TS waves

5.1. *Appearance of growing disturbances*

For small values of κ, numerical solutions of the boundary-region equations (4.1)–(4.5) reveal that for κ below a critical value κ_c, the disturbance appears to undergo exponential amplification for large $\bar{x}$. The value of κ_c depends on M. For $M = 3$, $\kappa_c \approx 0.03$. A growing disturbance is shown in figure 10 for $\kappa = 0.02$. Careful resolution checks were carried out to ensure that the solution is independent of the mesh sizes $\Delta\bar{x}$ and $\Delta\eta$ in the streamwise and normal directions, and that the growth is not a numerical instability. In order to examine the nature of the growing disturbance, the real and imaginary parts of the ratio $\bar{u}_x/\bar{u}$ ($\bar{u}_x \equiv \partial\bar{u}/\partial\bar{x}$) are also plotted in figure 10. Both $\mathrm{Re}(\bar{u}_x/\bar{u})$ and $\mathrm{Im}(\bar{u}_x/\bar{u})$ exhibit violent transient oscillations, but they finally become slowly varying functions of $\bar{x}$, suggesting that the growth is quasi-exponential and the disturbance has a well-defined local wavenumber and growth rate. After a substantial amplification, the disturbance reaches its peak and then decays. The erratic oscillation in the numerical result for the ratio $\bar{u}_x/\bar{u}$ occurs because $\bar{u}$ is extremely small before the exponential growth starts.

Such growing disturbances were not reported by LWG, presumably because they primarily focused on the cases with $\kappa = O(1)$, for which the spanwise viscous diffusion, which is proportional to κ^2, is strong enough to suppress the growth. For $\kappa < \kappa_c$, the boundary-region equations have to be integrated to very large distances to observe the

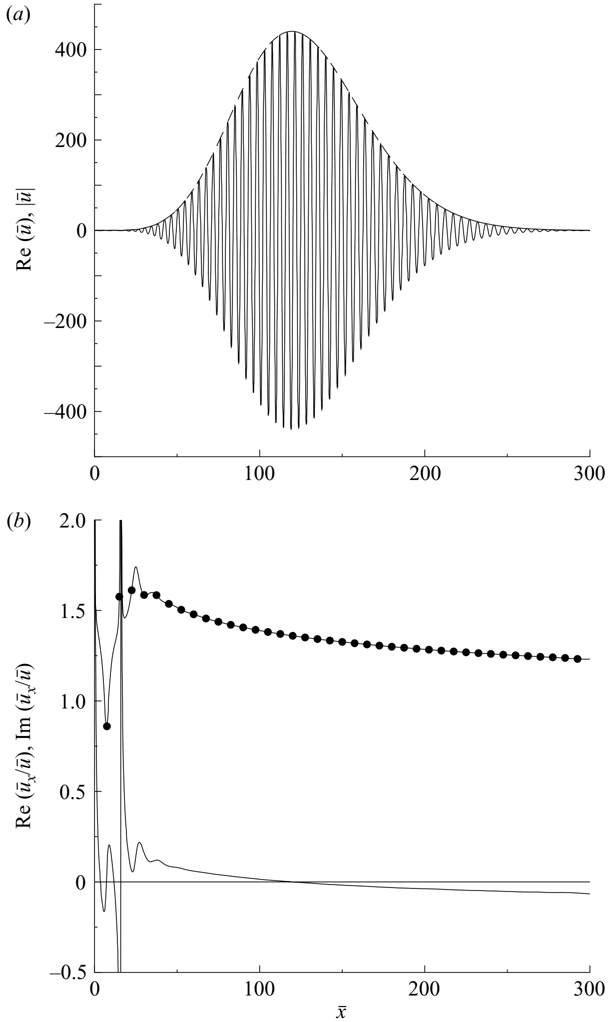

FIGURE 10. Appearance of growing disturbance for $M = 3$, $\kappa = \kappa_2 = 0.02$. (*a*) Re($\overline{u}$) and $|\overline{u}|$ *vs.* $\overline{x}$. (*b*) The real (solid line) and imaginary (solid line with circles) parts of the ratio $\overline{u}_x/\overline{u}$ *vs.* $\overline{x}$.

exponential growth. Indeed, the smaller the κ is, the farther downstream the growth starts. This is demonstrated in figure 11 for $M = 3$ and 4.5, where $\overline{x}_c$, the location where a disturbance starts to grow, is plotted against κ (with $\kappa_2 = \kappa$). Here, $\overline{x}_c$ is defined as the last position at which

$$\mathrm{Re}(\overline{u}_x/\overline{u}) = 0 \quad (\text{and } \mathrm{Re}(\overline{u}_x/\overline{u}) > 0 \text{ for } \overline{x} > \overline{x}_c). \tag{5.1}$$

The result for the incompressible case is not shown here because the growth occurs much farther downstream, with the earliest occurrence at $\overline{x} \approx 90$ for $\kappa = \kappa_c \approx 0.0125$.

The numerical solutions indicate that the scaled vertical wavenumber κ_2, which appears only in the outer boundary conditions (4.8)–(4.9), does not have an appreciable effect on $\overline{x}_c$ nor on the rate of growth, suggesting that the growing disturbance might be some unstable eigensolution excited by FST through a receptivity mechanism. The analysis to be presented below will confirm this

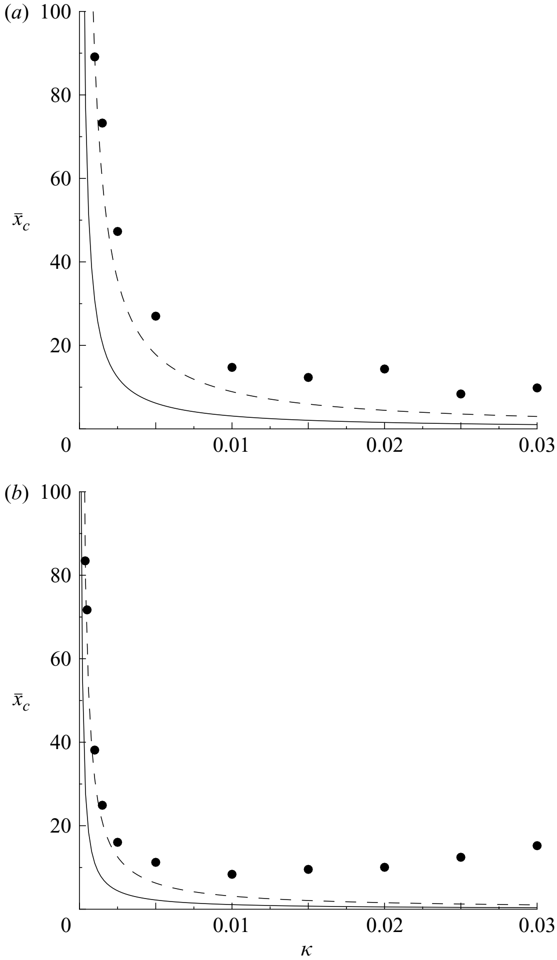

FIGURE 11. Onset location of growing disturbances $\bar{x}_c$ *vs.* κ for (*a*) $M = 3$ and (*b*) $M = 4.5$. Symbols: $\bar{x}_c$ extracted from the boundary-region solutions. Dashed lines: $\bar{x}_c$ predicted by (5.2) with c_0 determined by fitting with the point with the smallest κ. Solid lines: $\bar{x}_c$ predicted by (5.26).

speculation. It will show that $\bar{x}_c$ scales with κ as

$$\bar{x}_c \approx c_0/\kappa \tag{5.2}$$

for $\kappa \ll 1$, where c_0 depends on the Mach number.

5.2. *Quasi-three-dimensional Lam–Rott mode in BLEs*

To elucidate the nature of the growing disturbances observed numerically, we seek an asymptotic eigesolution of the unsteady boundary-region equations (4.1)–(4.5) in the double limits $\kappa \ll O(1)$ and $\bar{x} \gg O(1)$. The present three-dimensional system admits two classes of asymptotic eigensolutions. The first class is quasi-three-dimensional in the sense that the solutions depend on z, but have a zero spanwise velocity component. They are essentially identical to those first discovered by Lam & Rott (1960) and subsequently re-derived by Ackerberg & Phillips (1972) using a systematic matched asymptotic expansion. For completeness, we now describe these eigensolutions with a minor extension to include compressibility.

In the limit that $\overline{x} \gg 1$ and $\kappa \ll 1$, the asymptotic eigensolutions are proportional to $\exp(-\hat{\psi}\overline{x}^{3/2})$, where $\hat{\psi}$ is a complex constant (eigenvalue) to be found (cf. Ackerberg & Phillips 1972; Goldstein 1983). The boundary layer splits up into two decks: the main part of the boundary layer (or the main deck), and a thin viscous sublayer near the wall (or the lower deck). In the main deck $\eta = O(1)$, and it can be easily verified that

$$\{\overline{u}, \overline{v}, \overline{w}, \overline{\tau}\} = \left\{\frac{F''(\eta)}{T}, -\tfrac{3}{2}\hat{\psi}\sqrt{\overline{x}}F'(\eta), 0, -\frac{T'(\eta)}{T}\right\}\exp(-\hat{\psi}\overline{x}^{3/2}) + \dots \tag{5.3}$$

satisfy the leading-order balance in (4.1)–(4.5).

In the viscous sublayer, the inertia balances the viscous diffusion in the momentum equation. This determines the thickness of the layer to be $\eta = O(1/\sqrt{\overline{x}})$. We thus introduce

$$\zeta = \sqrt{\overline{x}}\eta = O(1)$$

and seek the solution of the form

$$\{\overline{u}, \overline{v}, \overline{w}\} = \left\{\overline{\overline{u}}(\zeta), \overline{\overline{v}}(\zeta), 0\right\}\exp(-\hat{\psi}\overline{x}^{3/2}) + \dots \tag{5.4}$$

The temperature fluctuation in this layer is smaller than that in the main layer by $O\left(1/\sqrt{\overline{x}}\right)$ and so there is no need to consider it. It follows from substituting (5.4) into (4.1)–(4.5) that $\left\{\overline{\overline{u}}, \overline{\overline{v}}, 0\right\}$ satisfies

$$-\tfrac{3}{2}\hat{\psi}\overline{\overline{u}} + \frac{\overline{\overline{v}}_\zeta}{T_w} = 0, \quad (-\mathrm{i} - \tfrac{3}{2}\hat{\psi}F''(0)\zeta)\overline{\overline{u}} + \frac{F''(0)}{T_w}\overline{\overline{v}} - \frac{\mu_w}{2T_w}\overline{\overline{u}}_{\zeta\zeta} = 0,$$

where μ_w and T_w denote the values of μ and T at the wall. The above equations can be written as the standard Airy equation in terms of the re-normalized variable

$$\hat{\zeta} = (3F''(0)\hat{\psi}T_w/\mu_w)^{1/3}\zeta + \zeta_0 \quad \text{with} \quad \zeta_0 = \mathrm{i}[(3F''(0)\hat{\psi})^2\mu_w/(8T_w)]^{-1/3}. \tag{5.5}$$

The solution for $\overline{\overline{u}}$ is found as

$$\overline{\overline{u}} = C\int_{\zeta_0}^{\hat{\zeta}} \mathrm{Ai}(\check{\zeta})\,\mathrm{d}\check{\zeta},$$

where Ai denotes the Airy function, C is a constant and ζ_0 must be a root of

$$\mathrm{Ai}'(\zeta_0) = 0 \tag{5.6}$$

in order to satisfy the boundary condition $\overline{\overline{u}}_{\zeta\zeta} = 0$ at the wall. The eigenvalue $\hat{\psi}$ is then related to ζ_0 by

$$\hat{\psi} = \frac{2^{3/2}\mathrm{e}^{\pi\mathrm{i}/4}}{3F''(0)\zeta_0^{3/2}}\left(\frac{T_w}{\mu_w}\right)^{1/2}.$$

The fact that the vertical velocity component in the main layer (see (5.3)) does not vanish as $\eta \to \infty$, implies that an upper deck must be introduced, where the normal velocity generates a pressure. The width of the upper deck must be of $O(\Lambda)$, i.e. $y \sim O(1)$, for the pressure to satisfy a Laplace equation (in the (y, z)-plane). From (3.2), (3.3) and (4.6), follows the estimate

$$\eta = O((\kappa\sqrt{\overline{x}})^{-1}). \tag{5.7}$$

By balancing the convective acceleration with the vertical pressure gradient in the y-momentum equation (4.3) in the upper deck, we find the induced pressure

$$\overline{p} \sim \frac{\overline{x}^{3/2}}{\kappa} \exp(-\hat{\psi}\overline{x}^{3/2}). \tag{5.8}$$

This pressure in turn generates a spanwise velocity in the lower deck, whose order-of-magnitude can be determined by balancing the inertia with the spanwise pressure gradient in the z-momentum equation (4.4), as follows

$$\overline{w} \sim \kappa\overline{x}^{3/2} \exp(-\hat{\psi}\overline{x}^{3/2}). \tag{5.9}$$

A key observation is that the displacement-induced pressure renders the inviscid and viscous motions interactive once $\overline{w}$ becomes sufficiently large to balance the dominant term $\partial\overline{u}/\partial\overline{x}$ in the continuity equation, that is

$$\overline{w} \sim \partial\overline{u}/\partial\overline{x} \sim \sqrt{\overline{x}}\exp(-\hat{\psi}\overline{x}^{3/2}).$$

Use of (5.9) gives

$$\overline{x} = O(\kappa^{-1}). \tag{5.10}$$

As will be shown in the next subsection, owing to the induced spanwise pressure gradient acting in the lower deck, a decaying Lam–Rott solution evolves into spatially growing, highly oblique TS-waves at the locations specified by (5.10).

The second class of eigensolutions have a non-zero spanwise velocity, but the normal velocity vanishes. It is easy to verify that in the viscous sublayer, the solution to leading-order can be expressed as

$$\{\overline{u}, \overline{v}, \overline{w}\} \sim \left\{\mathrm{Ai}(\zeta), 0, \tfrac{3}{2}\hat{\chi}\,\mathrm{Ai}(\zeta)\right\} \exp(-\hat{\chi}\overline{x}^{3/2}).$$

where ζ is defined by (5.5), but now ζ_0 is a root of $\mathrm{Ai}(\zeta_0) = 0$. The eigenvalue $\hat{\chi}$ is thus determined by $\hat{\chi} = \left(2^{3/2}\mathrm{e}^{\pi\mathrm{i}/4}\right)(3F''(0)\zeta_0^{3/2})/(T_w/\mu_w)^{1/2}$, and $\mathrm{Re}(\hat{\chi}) > 0$ since $\zeta_0 > 0$. Unlike the quasi-three-dimensional eigensolutions discussed earlier, the solutions of the second class decay exponentially as $\zeta \to \infty$. They are completely confined within the lower deck and hence do not produce any displacement effect to influence the outer flow. These solutions decay monotonically rather than evolving into TS waves.

5.3. *Triple-deck interactive regime and highly oblique TS waves*

In view of (5.10), we introduce the streamwise coordinate

$$x_1 = \kappa\overline{x} = O(1), \tag{5.11}$$

where $\kappa \ll 1$. An interactive triple-deck structure emerges, consisting of a lower deck ($\eta = O(\kappa^{1/2})$), a main deck ($\eta = O(1)$), and an upper deck ($\eta = O(\kappa^{-1/2})$).

In the main deck, the solution expands as

$$\{\overline{u}, \overline{v}, \overline{w}, \overline{p}, \overline{\tau}\} = \left\{u_1(x_1, \eta), \kappa^{-1/2}v_1(x_1, \eta), w_1(x_1, \eta), \kappa^{-5/2}p_1(x_1), \tau_1(x_1, \eta)\right\} E + \ldots, \tag{5.12}$$

where

$$E = \exp\left(\frac{\mathrm{i}}{\kappa^b}\int_0^{\overline{x}} \alpha_1(x_1)\,\mathrm{d}\check{x}\right).$$

The constant $b = 1/2$ is determined by balancing the inertia with the viscous term in the lower-deck x-momentum equation. Substituting (5.12) into (4.1)–(4.5) and solving the resulting equations at leading order, we obtain

$$\{u_1, v_1, w_1, \tau_1\} = \left\{A(x_1)F''/T,\ -\mathrm{i}\alpha_1 A(x_1)F',\ p_1(x_1)T/\left(\mathrm{i}\alpha_1 F'\right),\ -A(x_1)T'/T\right\}, \tag{5.13}$$

where $A(x_1)$ is an arbitrary function of x_1.

In the lower deck, we introduce

$$\boldsymbol{\eta} = \kappa^{-1/2}\eta = O(1). \tag{5.14}$$

The leading-order solution can be expressed as

$$\{\overline{u}, \overline{v}, \overline{w}, \overline{\tau}\} = \left\{\overline{u}_1(x_1, \boldsymbol{\eta}), \overline{v}_1(x_1, \boldsymbol{\eta}), \kappa^{-1/2}\overline{w}_1(x_1, \boldsymbol{\eta}), \kappa^{1/2}\overline{\tau}_1(x_1, \boldsymbol{\eta})\right\} E + \dots . \tag{5.15}$$

Inserting (5.15) into the boundary-region equations (4.1)–(4.4) yields

$$\left.\begin{aligned} \mathrm{i}\,\alpha_1\overline{u}_1 + \frac{1}{T_w}\frac{\partial \overline{v}_1}{\partial \boldsymbol{\eta}} + \overline{w}_1 = 0, \\ \mathrm{i}\left(-1 + F''(0)\alpha_1\boldsymbol{\eta}\right)\overline{u}_1 + \frac{F''(0)}{T_w}\overline{v}_1 = \frac{\mu_w}{2x_1T_w}\frac{\partial^2 \overline{u}_1}{\partial \boldsymbol{\eta}^2}, \\ \mathrm{i}\left(-1 + F''(0)\alpha_1\boldsymbol{\eta}\right)\overline{w}_1 = T_w p_1 + \frac{\mu_w}{2x_1T_w}\frac{\partial^2 \overline{w}_1}{\partial \boldsymbol{\eta}^2}. \end{aligned}\right\} \tag{5.16}$$

Eliminating p_1 from (5.16) shows that $\overline{v}_1$ satisfies

$$\left[\frac{\partial^2}{\partial \boldsymbol{\eta}^2} - \frac{2x_1T_w i}{\mu_w}\left(F''(0)\alpha_1\boldsymbol{\eta} - 1\right)\right]\frac{\partial^2 \overline{v}_1}{\partial \boldsymbol{\eta}^2} = 0, \tag{5.17}$$

which has the solution

$$\frac{\partial \overline{v}_1}{\partial \boldsymbol{\eta}} = \int_{\eta_0}^{\hat{\eta}} \mathrm{Ai}(\check{\eta})\,\mathrm{d}\check{\eta}, \tag{5.18}$$

where

$$\hat{\eta} = \left(2\mathrm{i}F''(0)\alpha_1x_1T_w/\mu_w\right)^{1/3}\boldsymbol{\eta} + \eta_0, \quad \eta_0 = -(\alpha_1F''(0))^{-1}\left(2\mathrm{i}F''(0)\alpha_1x_1T_w/\mu_w\right)^{1/3}.$$

Matching $\partial\overline{v}_1/\partial\boldsymbol{\eta}$ with the main-deck solution yields

$$\int_{\eta_0}^{\infty} \mathrm{Ai}(\check{\eta})\,\mathrm{d}\check{\eta} = -\mathrm{i}F''(0)\alpha_1A(x_1). \tag{5.19}$$

After setting $\boldsymbol{\eta} = 0$ in the x- and z-momentum equations and using the continuity equation, we obtain $\partial^3\overline{v}_1/\partial\boldsymbol{\eta}^3\big|_{\boldsymbol{\eta}=0} = (2x_1T_w^3/\mu_w)p_1$. Thus from (5.18), it follows that

$$\left(2\mathrm{i}F''(0)\alpha_1x_1T_w/\mu_w\right)^{2/3}\mathrm{Ai}'(\eta_0) = \frac{2x_1T_w^3}{\mu_w}p_1. \tag{5.20}$$

In the upper deck, the appropriate wall-normal variable is $\tilde{\eta} = \kappa^{1/2}\eta = O(1)$, and the solution expands as

$$\{\overline{u}, \overline{v}, \overline{w}, \overline{p}, \overline{\tau}\} = \left\{\kappa^{1/2}\tilde{u}_1(x_1, \tilde{\eta}), \kappa^{-1/2}\tilde{v}_1(x_1, \tilde{\eta}), \tilde{w}_1(x_1, \tilde{\eta}), \kappa^{-5/2}\tilde{p}_1(x_1, \tilde{\eta}), 0\right\} E + \dots \tag{5.21}$$

Inserting (5.21) into (4.1)–(4.4) leads to

$$\mathrm{i}\alpha_1\tilde{u}_1 + \frac{\partial\tilde{v}_1}{\partial\tilde{\eta}} + \tilde{w}_1 = 0, \quad \tilde{u}_1 = 0, \quad \mathrm{i}\alpha_1\tilde{v}_1 + \frac{1}{2x_1}\frac{\partial\tilde{p}_1}{\partial\tilde{\eta}} = 0, \quad \mathrm{i}\alpha_1\tilde{w}_1 - \tilde{p}_1 = 0. \tag{5.22}$$

These equations can be reduced to a Laplace equation for $\tilde{p}_1$

$$\frac{1}{2x_1}\frac{\partial^2 \tilde{p}_1}{\partial \tilde{\eta}^2} - \tilde{p}_1 = 0,$$

from which it follows that $\tilde{p}_1 = p_1(x_1)\exp\left(-\sqrt{2x_1}\tilde{\eta}\right)$. The vertical velocity behaves as $\tilde{v}_1 \to -\mathrm{i}p_1/(\alpha_1\sqrt{2x_1})$ for $\tilde{\eta} \to 0$, and matching it with the main-deck solution yields

$$p_1 = \alpha_1^2 A(x_1)\sqrt{2x_1}. \tag{5.23}$$

It follows from (5.19), (5.20) and (5.23) that (cf. Smith 1989; Wu 1999)

$$\Delta(x_1, \alpha_1) \equiv \int_{\eta_0}^{\infty} \mathrm{Ai}(\check{\eta})\,\mathrm{d}\check{\eta} - \frac{\mu_w^{1/3}}{T_w^{7/3}}\left(\frac{F''(0)}{\sqrt{2x_1}}\right)^{5/3}(\mathrm{i}\alpha_1)^{-1/3}\,\mathrm{Ai}'(\eta_0) = 0, \tag{5.24}$$

which is the dispersion relation to determine the complex wavenumber $\alpha_1 = \alpha_1(x_1)$. The above relation resembles the TS wave dispersion relation given, for example, by (3.17) in Wu (1999) and (5.29) later in this section. The difference is that the α_1^2 term (or equivalently α_{TS}^2 in Wu 1999) is absent because the streamwise pressure gradient, which contributes to that term, is neglected in the present framework of boundary-region equations. The eigensolution can be viewed as a highly oblique TS mode. Although M does not appear explicitly in (5.24), its influence enters implicitly through $F''(0)$, μ_w and T_w.

The integral term in (5.24) is associated with the spanwise pressure gradient induced by the viscous displacement. Obviously, as $x_1 \to 0$, this term vanishes so that the dispersion relation reduces to $\mathrm{Ai}'(\eta_0) = 0$, which implies that

$$\alpha_1 \to -\frac{(2x_1)^{1/2}\mathrm{e}^{-\pi\mathrm{i}/4}}{F''(0)\zeta_0^{3/2}}\left(\frac{T_w}{\mu_w}\right)^{1/2}.$$

It follows that

$$\frac{\mathrm{i}}{\kappa^{1/2}}\int_0^{\bar{x}} \alpha_1(x_1)\,\mathrm{d}\check{x} \to -\hat{\psi}\bar{x}^{3/2}. \tag{5.25}$$

This shows that a highly oblique TS wave matches to an upstream quasi-three-dimensional Lam–Rott mode or, in other words, the latter gradually evolves into a growing TS wave.

We computed the Airy function and its derivative using the method of Gil, Segura & Temme (2001). The complex wavenumbers are then obtained by solving the eigenrelation (5.24). The local growth rate and wavenumber are given by $-\mathrm{Im}(\alpha_1)/\kappa^{1/2}$ and $\mathrm{Re}(\alpha_1)/\kappa^{1/2}$, respectively. They can also be extracted from the numerical solution of the boundary-region equations, respectively, as $\mathrm{Re}(\bar{u}_x/\bar{u})$ and $\mathrm{Im}(\bar{u}_x/\bar{u})$. The theoretical and numerical results are now compared in figures 12 and 13 for a Mach 3 boundary layer. After an erratic transient phase, the disturbance acquires a well-defined wavenumber and growth rate, which vary slowly with $\bar{x}$. The growth rate is positive sufficiently downstream, indicating that there exist highly oblique growing modes despite the absence of the streamwise pressure gradient. For the case of $\kappa = 0.0025$ (figure 12), the predictions have the same trend, but the triple-deck result is obviously inaccurate quantitatively. The accuracy improves significantly when κ is reduced to $\kappa = 0.0005$ (figure 13), for which the error is about 20%. This is expected because the validity of asymptotic analysis is restricted to $\kappa \ll 1$. The corresponding onset location of growth moves further downstream, as anticipated by (5.10). Numerical solutions for somewhat high κ values (see e.g. figure 10) show

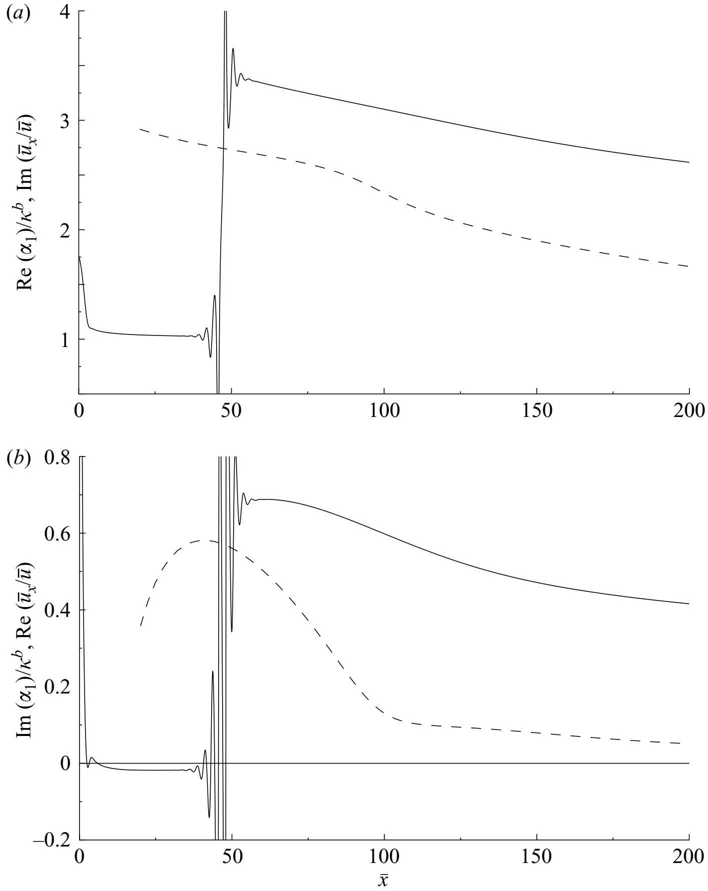

FIGURE 12. Comparison of (a) the local wavenumber and (b) growth rate of the growing disturbances for $M = 3$ and $\kappa = 0.0025$. The solid lines indicate the boundary-region solution and the dashed lines denote the triple-deck solution.

that the amplification is followed by decay, suggesting that there exists an upper branch of the unstable region. The upper branch cannot, however, be predicted by the triple-deck solution because it is associated with the curvature of the mean-flow profile (Bodonyi & Smith 1981), which is not accounted for in the triple-deck scaling regime.

Based on the broad agreement between the boundary-region solutions and the triple-deck theory, we may conclude that the growing disturbances are not a numerical artefact, but are highly oblique low-frequency TS waves, which are directly excited by the low-frequency three-dimensional components in the free-stream turbulence. The receptivity involved is akin to the well-known leading-edge adjustment mechanism (Goldstein 1983) in that the Lam–Rott eigensolution plays a key role. It is, however, also noticeably distinct from the latter because it is the spanwise rather than the streamwise pressure gradient that is instrumental in inducing the instability.

We may identify the onset location as the lower branch of the neutral curve. This means that in the triple-deck theory, $\overline{x}_c = x_1/\kappa$ with x_1 being the position at which

$$\mathrm{Im}\,(\alpha_1(x_1)) = 0. \tag{5.26}$$

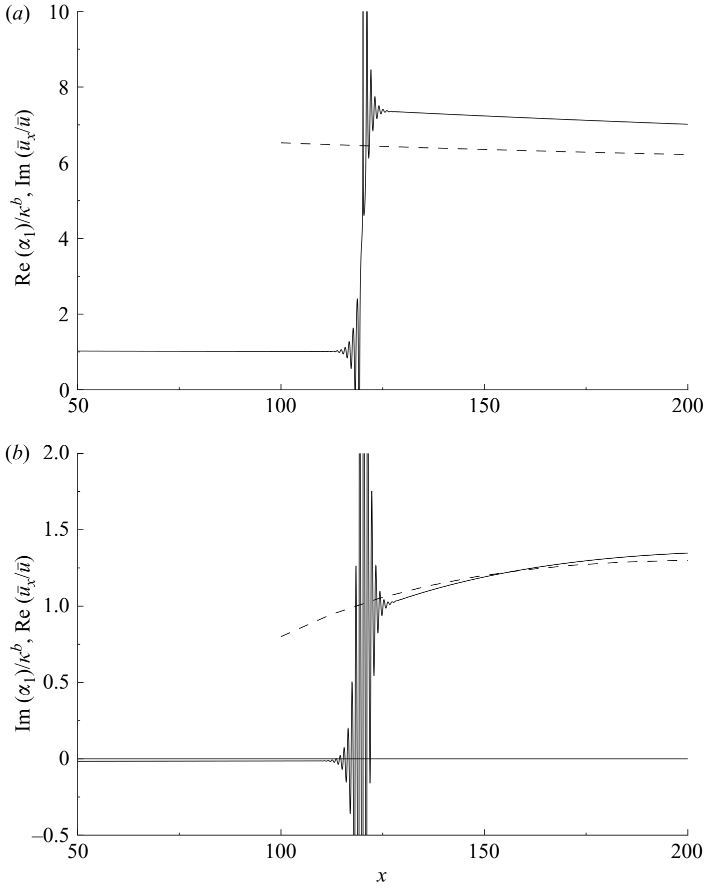

FIGURE 13. Comparison of (a) the local wavenumber and (b) growth rate of the growing disturbances for $M = 3$ and $\kappa = 0.0005$. The solid lines indicate the boundary-region solution and the dashed lines denote the triple-deck solution.

In figure 11, the onset location predicted by (5.26) is compared with that extracted from the boundary-region solution using (5.1). The former turns out to be much closer to the leading edge than the latter. Two factors may have contributed to this discrepancy. First, the triple-deck theory tends to predict a lower neutral Reynolds number (i.e. earlier onset) as it does in the two-dimensional case. Secondly, the criterion (5.1) yields a later onset because near the lower branch the signature of the eigensolution is exponentially small so that $\bar{u}$ can be 'masked' by a small inhomogeneous part of the solution. A consistent local growth rate and wavenumber can be extracted only after the TS wave has already undergone substantial amplification. For the same reason, the gradual wavelength shortening process of the Lam–Rott eigensolutions cannot be observed in the numerical solution.

In reality, both the streamwise and spanwise pressure gradients are induced. It is thus of interest to determine the respective conditions under which these two mechanisms operate. The flow becomes interactive via the streamwise pressure gradient when the latter balances the inertia in the lower-deck x-momentum equation. In order to estimate the locations at which this occurs, we consider the linearized

Navier–Stokes equations, in which the mentioned balance is

$$(k_3/k_1)F'\partial\bar{u}/\partial\bar{x} \sim (k_3/R_\Lambda)\partial\bar{p}/\partial\bar{x}.$$

Noting that $F' \sim O(1/\sqrt{\bar{x}})$ and using (5.4) and (5.8), we deduce that

$$\bar{x} = O\big(R_\Lambda^{1/4}/k_1^{3/4}\big). \tag{5.27}$$

For the mechanism of the spanwise pressure gradient to be physically relevant, the location given by (5.27) must be much farther downstream than that specified by (5.10), that is $R_\Lambda^{1/4}/k_1^{3/4} \gg 1/\kappa$, yielding $k_1 \ll R_\Lambda^{-1/5}$. Meanwhile, the condition $\kappa \ll 1$ must hold, which requires $k_1 \gg R_\Lambda^{-1}$. It can now be concluded that the receptivity mechanism triggered by the spanwise pressure gradient operates for external disturbances with frequencies in the range

$$R_\Lambda^{-1} \ll k_1 \ll R_\Lambda^{-1/5}. \tag{5.28}$$

The streamwise pressure gradient renders the boundary layer unstable if $k_1 \gg O(R_\Lambda^{-1/5})$. We can easily include both scenarios by adapting the generic scaling $k_1 = O(R_\Lambda^{-1/5})$, for which the generated TS waves have comparable streamwise and spanwise wavelengths, both of $O(\Lambda)$. By letting $k_1 = \hat{k}R_\Lambda^{-1/5}$ and reinstating the streamwise pressure gradient in (4.1)–(4.4), we derive the dispersion relation (cf. Smith 1989; Wu 1999)

$$\int_{\eta_0}^{\infty} \mathrm{Ai}(\breve{\eta})\,\mathrm{d}\breve{\eta} - \frac{\left[1+(1-M^2)(\alpha_1\hat{s})^2\right]^{1/2}}{1+(\alpha_1\hat{s})^2}\,\frac{\mu_w^{1/3}}{T_w^{7/3}}\left(\frac{F''(0)}{\sqrt{2x_1}}\right)^{5/3}(\mathrm{i}\alpha_1)^{-1/3}\,\mathrm{Ai}'(\eta_0) = 0, \tag{5.29}$$

where $\hat{s} = \hat{k}^{5/4}/k_3^{3/2}$. The relative role of the streamwise and spanwise pressure gradients is characterized by $\hat{s}$ (or equivalently $\hat{k}$). When $\hat{k} = 0$, only the spanwise pressure gradient is active for the growth and the above relation reduces to (5.24). When $\hat{k} = O(1)$, the pressure gradients have comparable influence on the growth. When $\hat{k} \gg 1$, the streamwise pressure gradient is dominant in inducing the instability. Solutions for (5.29) for $\hat{k} = 5$ and 10 are presented in figure 14. The comparison with those for $\hat{k} = 0$ suggests that for $\hat{k} = 10$ (or $\hat{s} = 1.13$) the streamwise pressure gradient typically causes a difference smaller than 10%, indicating that the spanwise pressure gradient is dominant.

It would be interesting to study experimentally the generation of such highly oblique, low-frequency TS waves in the compressible regime by using controlled free-stream vortical disturbances (cf. Dietz 1999). In order to aid future laboratory study as well as to illustrate the potential relevance of these TS waves in practical situations, the locations where these waves are expected to be observed, denoted by x_c^*, are estimated in dimensional form. We consider the cases of $M = 0.8$ and $M = 3$, for both laboratory and flight conditions. The free-stream velocity and kinematic viscosity are given in table 4. For flight conditions, these are calculated by assuming the temperature and density at a typical cruise height of 10 km above sea level.

Since both the boundary-region solutions and the triple-deck analysis suggest that $\bar{x}_c \sim \kappa^{-1}$ for $\kappa \ll O(1)$ and that $\bar{x}_c$ is more or less constant for $\kappa \sim O(1)$, it follows that $x_c^* \sim O(\sqrt{R_\Lambda/k_1}\Lambda)$ or $x_c^* \sim O(k_1^{-1}\Lambda)$, implying that higher-frequency disturbances tend to appear earlier. We take k_1 corresponding to $\hat{k} = 10$, for which the instability is primarily induced by the spanwise pressure gradient as figure 14 indicates. For a fixed $\hat{k}$, the criteria for oblique TS waves to occur, namely $\kappa < \kappa_c$ and $k_1 < \hat{k}R_\Lambda^{-1/5}$, require Λ to be greater than a critical value Λ_c. The minimal values

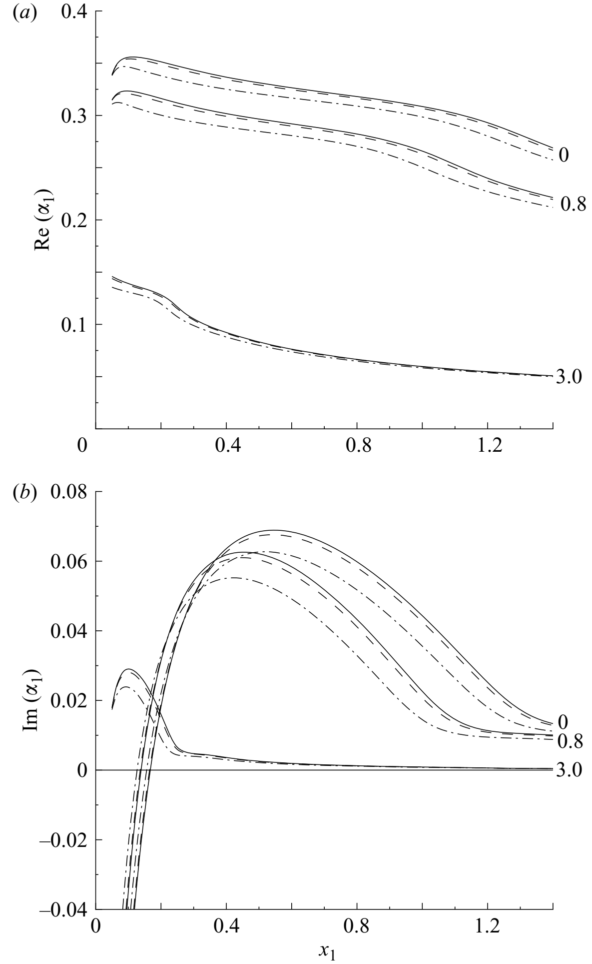

FIGURE 14. Solutions to (5.29) for different values of $\hat{k}$ showing the effect of the streamwise pressure on (a) the local wavenumber and (b) growth rate of the growing disturbances. Solid lines: $\hat{k} = 0$, dashed lines: $\hat{k} = 5$ and dash-dotted lines: $\hat{k} = 10$. Numbers in the graphs indicate the Mach number.

with $\hat{k} = 10$ are displayed in table 4. For laboratory condition at $M = 0.8$ and $M = 3$, $\Lambda_c \approx$ 1–2 cm, whereas, for a Mach 3 flight condition, $\Lambda_c \approx 2$ mm. In each case, the corresponding x_c^* represents the earliest position where a TS wave with frequency f^* starts to amplify.

The amplification location of the excited TS wave depends on Λ, which may be quite different in laboratory and flight conditions. The onset locations for some plausible values of Λ and the frequencies of the TS waves (corresponding to $\hat{k} = 10$) are given in table 5. The choices of Λ are based on the following considerations. In the laboratory, grids are often used to reduce Λ. For $M = 0.8$, we take $\Lambda = 0.01$ m, the same as in Kendall's experiments. For $M = 3$, $\Lambda = 0.01$ m would be smaller than the required minimum $\Lambda_c = 0.0165$ m, and so $\Lambda = 0.02$ m is chosen instead. Note also that the kinematic viscosity changes significantly in the two cases because for $M = 0.8$ we have assumed atmospheric conditions, while for $M = 3$ the conditions correspond to the pressurized tunnel of Graziosi & Brown (2002). The data in table 5 suggest

Case	U_∞ (m s^{-1})	ν $\left(\mathrm{m}^2\ \mathrm{s}^{-1}\right)$	Λ_c (m)	x_c^* (m)	f^* (Hz)
$M = 0.8$ – Lab	276.8	1.550×10^{-5}	0.0072	0.50	5648.67
– Flight	239.6	3.962×10^{-5}	0.0212	1.43	1709.53
$M = 3.0$ – Lab	620.7	2.861×10^{-4}	0.0165	0.13	7336.47
– Flight	892.3	3.962×10^{-5}	0.0016	0.01	108 046.70

TABLE 4. Minimal spanwise length scales Λ_c to satisfy the criterion $\kappa < \kappa_c$ with $\hat{k} = 10$ in $M = 0.8$ and 3.0 boundary layers. A TS wave with frequency f^* starts to amplify from x_c^*.

Case	Λ (m)	R_Λ	κ	k_1	$\overline{x}$	x_c^* (m)	f^* (Hz)	σ_1	σ_2
$M = 0.8$ – Lab	0.01	178 580.65	0.0158	0.8904	63.75	0.716	3922.58	0.163	2813.72
– Flight	0.06	362 835.71	0.0119	0.7727	69.47	5.395	491.00	0.106	4305.32
$M = 3.0$ – Lab	0.02	43 385.83	0.0277	1.1817	9.16	0.155	5836.50	0.145	1203.89
– Flight	0.06	1 351 563.04	0.0070	0.5940	22.07	2.229	1406.11	0.073	9477.24

TABLE 5. Typical dimensional onset locations of growth in $M = 0.8$ and 3 boundary layers. $\sigma_1 = (k_1/k_3)\mathrm{Im}(\overline{u}_x/\overline{u})$ and $\sigma_2 = 2\pi R_\Lambda^{3/5}/(\hat{k}\overline{x})^{1/2}$.

that in Mach 0.8 and Mach 3 boundary layers, growing TS waves may be observed in the laboratory within about 1 m and 20 cm from the leading edge, respectively.

In flight conditions, Λ is likely to be larger than in laboratory conditions. Lacking the precise data, we take $\Lambda = 0.06$ m. For $M = 0.8$, TS waves would start to grow at about 5.4 m from the leading edge. They are expected to be relevant only for transition over a fuselage. For $M = 3$, amplification starts from $x_c^* \approx 2.5$ m. However, if a significant level of relatively short length-scale disturbances is present, the onset position shifts upstream, e.g. to 1.5 m for $M = 0.8$ (see table 4). In table 5, we also give σ_1, the ratio of the spanwise wavelength to the streamwise wavelength of the excited TS waves, which shows that these are highly oblique waves. The last column in table 5, σ_2, is the ratio of the streamwise wavelength of the free-stream vortical disturbances to the local boundary-layer thickness at the onset position. Obviously, the relevant disturbance components are of sufficiently long wavelength that the boundary-region equations are applicable.

In the incompressible case, if we take $\Lambda = 0.01$ m as in Kendall's experiments, then for a typical low-speed wind-tunnel experimental condition $M = 0.08$, $\kappa > \kappa_c$, that is, no growing TS wave can be induced by the spanwise pressure gradient alone in this case. For $\hat{k} = 10$, the smallest Λ to satisfy $\kappa < \kappa_c$ is $\Lambda \approx 0.2$ m, and this yields $x_c^* = 22.7$ m. Clearly, not only is this distance too large to be of any practical relevance, the required Λ far exceeds the typical values for FST. The onset location shifts upstream for smaller Λ if $\hat{k}$ is substantially increased, but then the streamwise pressure gradient becomes dominant.

As a summary of the discussions above, it may be concluded that highly oblique low-frequency TS waves can be generated by FST primarily by the spanwise pressure gradient mechanism at sufficiently high subsonic ($M > 0.8$) to supersonic speeds in both laboratory and flight conditions. It is, however, not a dominant receptivity mechanism in the low-Mach-number subsonic regime.

When a boundary layer is subjected to various components of different frequencies (i.e. k_1) in the FST, the ensuing response can be summarized by figure 15. For

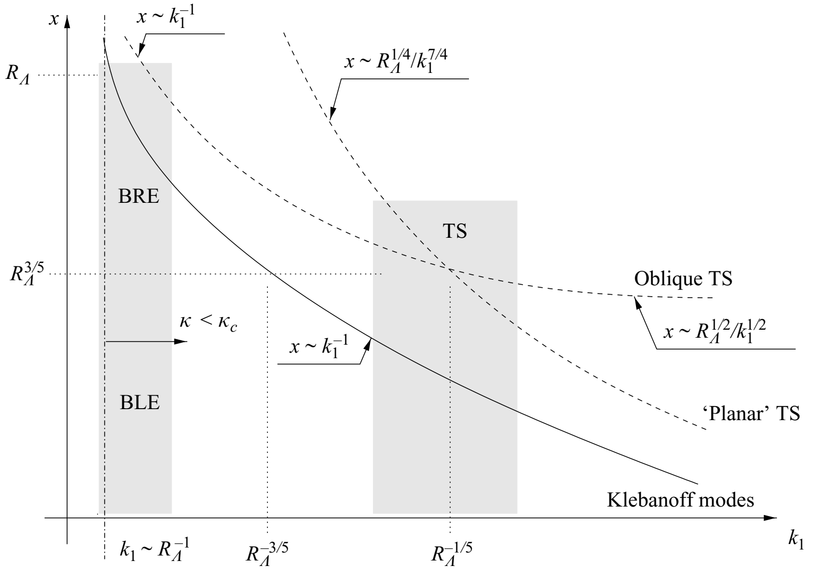

FIGURE 15. Flow response regimes.

simplicity, all components are assumed to have the same spanwise length scale Λ. Klebanoff modes or streaks, which correspond to the inhomogeneous part of the solution, always appear first, at locations $x \sim k_1^{-1}$. If the FST level is sufficiently high, they may reach or exceed the threshold magnitude to cause secondary instability, thereby leading to bypass transition. However, if the FST level is moderate, the induced streaks eventually decay, but the homogeneous part of the solution, i.e. the Lam–Rott eigenmodes excited by FST, can evolve into TS waves so that the conventional transition route prevails. For $k_1 \gg R_\Lambda^{-1/5}$, the instability is primarily induced by the self-induced streamwise pressure gradient and occurs at locations $x \sim R_\Lambda^{1/4}/k_1^{7/4}$. The scenario is essentially two-dimensional and so is labelled as 'planar TS' in the diagram. For $R_\Lambda^{-1} \ll k_1 \ll R_\Lambda^{-1/5}$, the Lam–Rott modes develop into highly oblique TS waves, for which the self-induced spanwise pressure gradient is the dominant mechanism of instability. The scaling $k_1 \sim R_\Lambda^{-1/5}$ is distinguished in that both effects are included. Although the streaks and the TS wave appear in sequence when a single component is present, they may coexist at the same streamwise region if more than one component is present. For instance, if the free stream consists of components with $k_1 \sim R_\Lambda^{-1/5}$ and $k_1 \sim R_\Lambda^{-3/5}$, then the former will excite a TS wave whilst the latter will generate streaks in the same region $x \sim R^{3/5}$. A mutual interaction can take place between these two types of motions. Such an interaction, which is highly likely given the broadband nature of FST, may be related to the effect of FST on TS waves and warrants further investigation.

6. Root mean square of fluctuations inside the boundary layer

The free-stream turbulence can be represented by a superposition of a continuous band of Fourier components. Owing to the linear nature of the disturbances, the fluctuations induced within the boundary layer can be computed by a proper summation of the contribution of each Fourier component. The boundary-layer response can then be characterized by the r.m.s. of the relevant fluctuating quantities.

LWG showed that the mean-square streamwise velocity fluctuation produced by a broadband free-stream turbulence, is given by

$$\langle u'^2\rangle(R_\Lambda,\eta,\delta)=\frac{R_\Lambda}{\delta^2}\int_0^\infty \Phi_t(k_1=0,\xi/\delta)K_\infty(\xi,\eta)\xi\,\mathrm{d}\xi, \tag{6.1}$$

where $\epsilon u'\equiv u-F'$, $\langle\rangle$ denotes the mean value, and

$$K_\infty(\xi,\eta;M)=2\int_0^\infty\int_0^{2\pi}\frac{\sin^2\theta}{s^2}|\bar{u}(\bar{x},\eta,\theta,s)|^2\,\mathrm{d}\theta\,\mathrm{d}s. \tag{6.2}$$

Here ξ, θ and s are related to k_2, k_3 and $\bar{x}$ via the relations

$$k_2=\frac{\xi}{\delta}\cos\theta,\quad k_3=\frac{\xi}{\delta}\sin\theta,\quad \bar{x}=\xi^2 s/2\quad (\text{with}\quad \delta=\sqrt{2x/R_\Lambda}),$$

from which it follows that

$$\xi=\delta\sqrt{k_2^2+k_3^2},\quad \kappa=\sin\theta/\sqrt{s},\quad \kappa_2=\cos\theta/\sqrt{s},\quad s=k_1R_\Lambda\delta^2/\xi^2. \tag{6.3a–d}$$

In (6.1), $\Phi_t(k_1=0,\xi/\delta)$ is the spanwise spectral function describing the statistical property of the FST upstream of the leading edge. We have put $k_1=0$ because low-frequency components dominate the core of the boundary layer. Lacking well-documented spectral data about the FST in the compressible experiments, we shall employ a particular form of function Φ_t, used by LWG to model Kendall's experiments, namely

$$\Phi_t(0,\xi/\delta)=\frac{C\langle u_\infty^2\rangle}{\pi^2\delta^2}\xi^2\exp(-(\xi/\delta-\bar{k}_I)^2/\Delta), \tag{6.4}$$

where $\Delta=4.0$, $\bar{k}_I=-7.0$, and C is determined by following LWG. This spectrum is concentrated around a specific spanwise wavenumber, which accounts for the fact that the boundary-layer signature exhibits a discernible spanwise periodicity.

In the compressible case, FST generates temperature fluctuations and its mean-square value is given by

$$\langle\tau'^2\rangle(R_\Lambda,\eta,\delta)=\frac{R_\Lambda}{\delta^2}\int_0^\infty \Phi_t(k_1=0,\xi/\delta)K_\tau(\xi,\eta)\xi\,\mathrm{d}\xi, \tag{6.5}$$

where K_τ is given by (6.2), but with $\bar{u}$ being replaced by $\bar{\tau}$. A similar expression, K_m, can be derived for the mean-square values of mass-flux fluctuations.

In experiments, the r.m.s. in a specific frequency band $\{k_{1L},k_{1H}\}$ is often measured. A theoretical prediction requires changing the limits of the integral (6.2) with respect to variable s, that is, K_∞ must be replaced by $K_{\langle\rangle}$, defined as

$$K_{\langle\rangle}(\xi,\eta;\delta,R_\Lambda,k_{1L},k_{1H})=2\int_{s_L}^{s_H}\int_0^{2\pi}\frac{\sin^2\theta}{s^2}|\bar{u}(\bar{x},\eta,\theta,s)|^2\,\mathrm{d}\theta\,\mathrm{d}s, \tag{6.6}$$

where

$$s_L=k_{1L}R_\Lambda\delta^2/\xi^2,\qquad s_H=k_{1H}R_\Lambda\delta^2/\xi^2.$$

For the temperature and mass flux, on replacing $|\bar{u}|$ by $|\bar{\tau}|$ and $|\overline{\rho u}|$, respectively, similar functions can be defined, which can be used in (6.1) to calculate mean-square values of the respective quantities.

To evaluate K_∞, we write

$$K_\infty(\xi,\eta;M)=2\int_0^{s_\infty}\int_0^{2\pi}\frac{\sin^2\theta}{s^2}|\bar{u}(\bar{x},\eta,\theta,s)|^2\,\mathrm{d}\theta\,\mathrm{d}s, \tag{6.7}$$

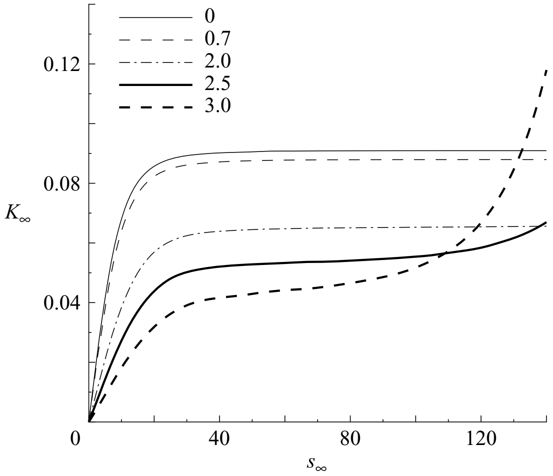

FIGURE 16. Function $K_\infty = K_\infty(\xi = 1, \eta = 1.64)$ as a function of the upper limit s_∞ for different Mach numbers.

where the upper limit of the integration with respect to s must be sufficiently large. The fact that $\bar{u}$ evolves into an instability mode downstream for small κ means that, for K_∞ to be convergent, s_∞ must be so large that the corresponding $\bar{x}$ must extend beyond the upper branch of the growing disturbances. This computational demand makes the evaluation of K_∞ impossible in practice. In the following, we shall show that for the purpose of calculating the r.m.s. of broadband fluctuations with growing disturbances being excluded, a somewhat modified K_∞ is defined.

According to the numerical finding in §6, $\bar{u}$ in the integrand would correspond to a growing mode if s is sufficiently large that

$$\bar{x} = \tfrac{1}{2}\xi^2 s > \bar{x}_c = c_0/\kappa \quad \text{and} \quad \kappa = \sin\theta/\sqrt{s} < \kappa_c,$$

i.e. if

$$s > \max\left(\sin^2\theta/\kappa_c^2,\ 4c_0^2/\left(\xi^4 \sin^2\theta\right)\right).$$

The minimum of the right-hand side, attained when $\sin^2\theta = 2c_0\kappa_c/\xi^2$, is $2c_0/(\kappa_c\xi^2)$. Hence, for the integral not to include signatures of growing modes, the largest upper limit s_∞ is

$$s_\infty = 2c_0/\left(\kappa_c\xi^2\right).$$

On using (6.3d), we note that the integral (6.7) includes the contribution of all disturbances with frequencies up to k_1 given by

$$k_1 = 2c_0/(\kappa_c R_\Lambda \delta^2),$$

while neglecting the contribution of the components with higher frequencies.

Figure 16 shows the variation of K_∞ with the upper limit s_∞ for $\xi = 1$. For M up to 3, K_∞ develops a well-defined plateau between $s = s_L$ and s_R. This implies that the boundary layer is primarily responsive to components in a well-defined low-frequency band whereas the components beyond that band (but still below the lower end of the characteristic frequencies of the instability) generate little response. The saturated value may be defined as K_∞, although strictly speaking the integral is not yet convergent. Such a modified K_∞ may be used in (6.1) to compute the r.m.s. value of 'broadband' disturbances without including the excited growing instability

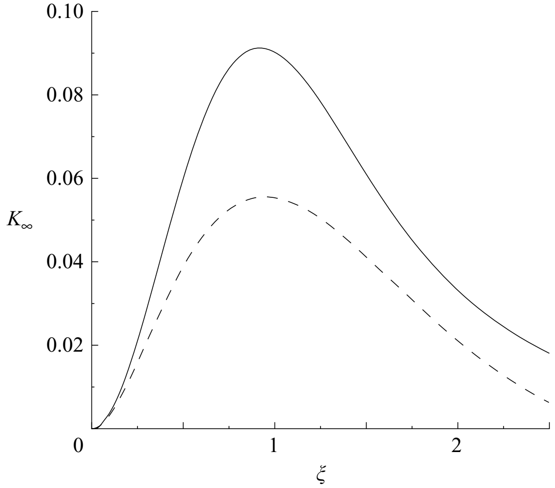

FIGURE 17. Function $K_\infty = K_\infty(\xi, \eta = 1.64)$ for the broadband case. The solid line indicates the result of the present analysis whereas the dashed line denotes the result by LWG.

modes. For $M > 3$, the plateau disappears and it is no longer possible to define an appropriate K_∞ without including the excited TS waves in the integral. Computing the r.m.s. of broadband disturbances becomes practically impossible. In this case, it is better to compute the r.m.s. in a specified frequency band by using (6.6).

Figure 17 depicts the function $K_\infty(\xi, \eta)$ computed as described above for the incompressible case; here $\eta = 1.64$, which is the approximate location of the maximum of the streamwise velocity fluctuation. The result is compared with that of LWG. Our curve lies above theirs. No apparent reason has been found for this disagreement. This discrepancy further motivated us to perform checks of the independence of our solution on the computational parameters including the size and resolution of the integral domain as well as the step size in the streamwise direction and the mesh size in the vertical direction.

Figure 18 shows K_∞ for $M = 0$, $M = 1.5$ and $M = 3$. For the purpose of predicting the mean-square value of the mass-flux fluctuation, which is the quantity that is readily measured in experiments, we have also computed K_m. The shapes of the two functions look similar.

6.1. *Incompressible flow: comparison with the data of Kendall*

Since our calculations lead to somewhat larger values of K_∞ than those in LWG, we recalculated the result presented in figure 10 of LWG and again compared the numerical results with the (unpublished) data of Kendall, also shown by LWG. The oncoming free-stream speed is $U_\infty = 11.6$ m s^{-1}. The FST is characterized by $\Lambda = 0.009$ m and a spanwise free-stream turbulence level of 0.26%. Figure 19 shows the r.m.s. of the streamwise velocity fluctuation at $\eta = 1.64$ as a function of the boundary-layer thickness δ for different frequency bands. Consistent with the fact that our calculations give higher values for the function K_∞, the broadband r.m.s. is higher than that obtained by LWG. Note that although our values of K_∞ are larger than those of LWG by more than 30%, the difference in the r.m.s. is much smaller. This is because K_∞ is weighted by the spectrum function Φ_t (see (6.1)), which decays quickly with ξ. Among the three selected frequency intervals, the r.m.s. within the low-frequency band (0–4 Hz) agrees best with the experimental data, confirming

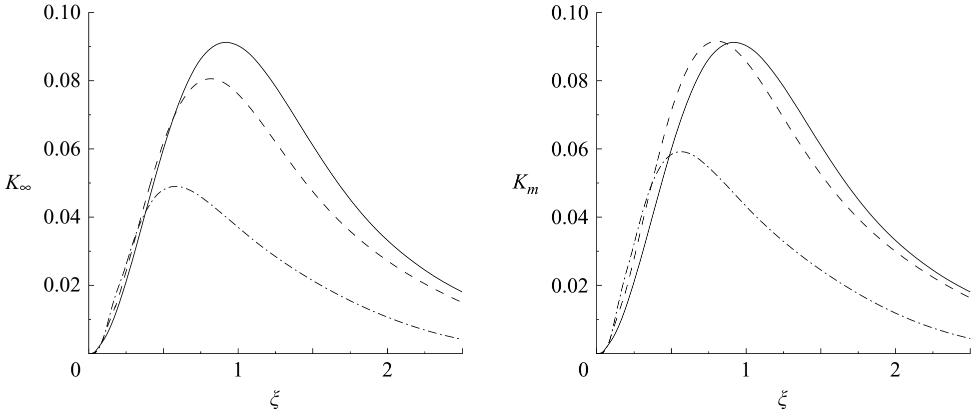

FIGURE 18. Functions K_∞ and K_m *vs*. ξ for $\eta = 1.64$. Solid line: $M = 0$, dashed line: $M = 1.5$ and dash-dotted line: $M = 3.0$.

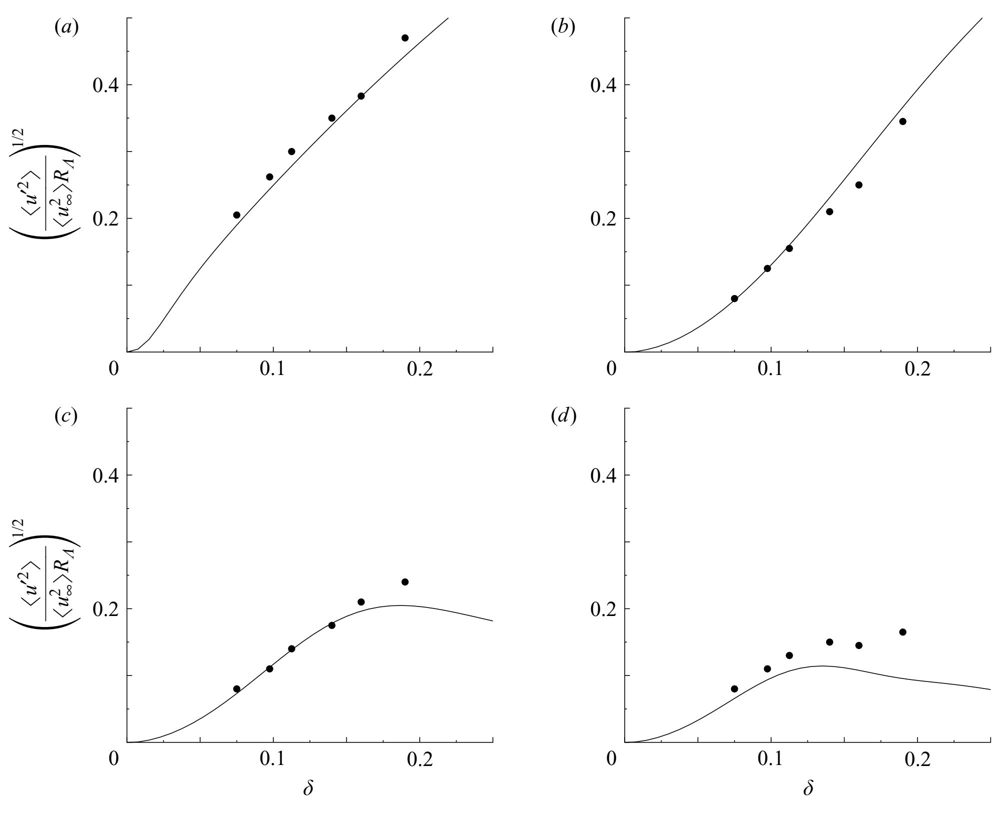

FIGURE 19. Experimental data by Kendall (as quoted in LGW) and the corresponding numerical results. (a) Broadband r.m.s.; (b) r.m.s. for $f^* = \{0, 4\}$ Hz; (c) r.m.s. for $f^* = \{4, 8\}$ Hz and (d) r.m.s. for $f^* = \{8, 12\}$ Hz.

that the boundary-region equations are well suited for describing the fluctuations at low frequencies. Our results seem to fit the experimental data somewhat better than those of LWG, especially for the two relatively high bands. The order of magnitude of the fluctuations is captured with satisfactory accuracy for the frequency ranges

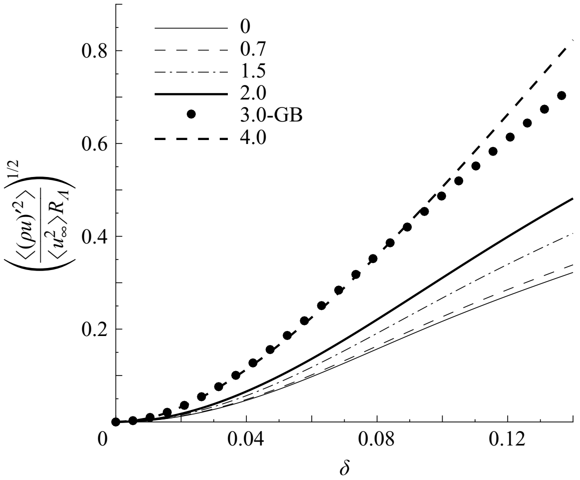

FIGURE 20. Downstream evolution of the r.m.s. of mass flux fluctuation in the frequency range $f^* = \{0, 18\}$ Hz (represented by the curves) for different Mach numbers. The symbols represent the r.m.s. in the frequency range $f^* = \{0, 1000\}$ Hz pertaining to the experimental condition of Graziosi & Brown (2002). The wall-normal positions correspond to the maximum of fluctuations and are: $\eta = 1.64$ ($M = 0.0$), $\eta = 1.73$ ($M = 0.7$), $\eta = 2.02$ ($M = 1.5$), $\eta = 2.20$ ($M = 2.0$), $\eta = 2.47$ ($M = 3.0$), $\eta = 2.66$ ($M = 4.0$).

4–8 Hz and 8–12 Hz. However, this apparent improvement should be viewed with caution because uncertainties exist in both the measurement and the input spectrum. The agreement with the experimental data progressively deteriorates as the frequency increases. This is expected because, as a consequence of neglecting the streamwise pressure and diffusion terms, the LUBR equations cannot describe high-frequency disturbances, which is the major limitation of this approach.

6.2. *Effect of Mach number*

The influence of Mach number on the downstream evolution of the r.m.s. of the mass flux fluctuation inside the boundary layer is investigated. Lacking reliable information about the FST spectrum in the compressible regime, the spectrum given by (6.4) is used. The Mach number is varied by changing U_∞ while keeping c_∞ (calculated for the ground condition) constant. We choose to calculate the r.m.s. in the frequency window $\{0 - 18\}$ Hz so that, in the incompressible limit, it consists of disturbances with frequencies below those of the TS waves (typically 30–150 Hz in wind-tunnel experiments). For a Mach 3 boundary layer, the band actually consists of only a small fraction of disturbances which could have been considered as ‘low-frequency’ since the characteristic frequencies of instability increase. The position at which the r.m.s. attains its maximum value increases notably with the Mach number, but varies only slightly with the downstream location. Therefore, for each Mach number, we choose the η value of the maxima at a vanishingly small x. As shown in figure 20, compressibility, as measured by M, enhances the r.m.s. This behaviour is expected because the mass flux increases with the Mach number for each Fourier mode in the low-frequency range.

As a demonstration that for higher Mach numbers we can include components within a much broader (dimensional) frequency band, we consider specifically the pressurized wind-tunnel experiments of Graziosi & Brown (2002), in which the frequencies of the unstable modes are centred at about 10 kHz. The r.m.s. of the mass-flux fluctuation in range of $\{0-1000\}$ Hz is shown in figure 20. Unfortunately, we are unable to find suitable experimental data to carry out a quantitative comparison.

7. Conclusions

In this paper, we have investigated how a compressible laminar boundary layer responds to small-amplitude free-stream disturbances of the convected-gust type. For the long-wavelength (low-frequency) components of relevance, the linearized unsteady boundary-layer and boundary-region equations, which constitute rigorous asymptotic limits of the full Navier–Stokes equations, have been employed to describe the entrainment of FST and the development of the induced fluctuations within the boundary layer.

Similarly to the incompressible case studied by Leib *et al.* (1999), the response predominantly consists of low-frequency fluctuations. In the low-Mach-number regime, the unsteady flow within the boundary layer is characterized by streamwise-elongated low-frequency velocity streaks (i.e. Klebanoff modes). Increasing the Mach number generally enhances the temperature and mass-flux fluctuations, but the effect of compressibility on the velocity fluctuation is complex: the velocity response may either be enhanced or inhibited, depending on the streamwise locations and frequencies.

A significant feature of a compressible boundary layer is that free-stream vortical disturbances induce intense temperature fluctuations even for moderate Mach numbers, leading to the formation of thermal streaks. The conventional concept of streak instability might thus need to be re-examined. It is likely that the temperature field has to be included in the formulation of secondary instability.

Another finding of the present study is that FST can generate highly oblique low-frequency TS instability waves through a modified leading-edge adjustment receptivity mechanism. The excitation involves wavelength shortening of a quasi-three-dimensional Lam–Rott boundary-layer eigensolution to produce a spanwise pressure gradient. The latter in turn interferes with the viscous flow in a thin viscous sublayer near the wall, thereby causing the initially decaying Lam–Rott eigenmode to evolve into a spatially growing TS wave. In the supersonic speed regime $M > 3$, this mechanism operates in the region close to the leading edge. These results shed some new light on how FST may influence the evolution of a compressible laminar boundary layer and its eventual breakdown.

We end this paper by pointing out a number of related topics for further investigation. The first is concerned with calculating the boundary-layer signature induced by free-stream acoustic disturbances, which are particularly strong in wind-tunnel experiments. The same framework of boundary-layer/region equations may still be used and the computational results may be validated by a detailed quantitative comparison with the well-documented experimental data (Graziosi & Brown 2002). The second topic is to extend the present linear formulation to include nonlinear interactions among the Fourier components and to carry out the related numerical calculations. A secondary instability analysis can subsequently be performed. As these streaks are driven by and quantitatively related to the naturally present FST, the calculation would yield an estimate of the required threshold intensity of FST for secondary instability. Such a result would be crucial for delineating the bypass transition and usual transition route, and hence be of direct engineering relevance. Finally, the present theoretical framework may be combined with DNS to formulate an efficient hybrid approach to bypass transition. The computational domains in the existing DNS studies usually start some distance downstream the leading edge and the inflow conditions have hitherto been specified in terms of the continuous spectra of the Orr–Sommerfeld and Squire operators. However, these spectra do not satisfactorily represent the disturbances which have penetrated into the boundary layer upstream because the non-parallel effect, which actually plays a crucial role for the entrainment of the most relevant long-wavelength free-stream disturbances, has been neglected. In contrast, the boundary-region equations successfully describe this early response to the FST in the upstream region. The solution to these equations may be used to provide the appropriate inlet conditions for DNS.

P.R. would like to thank Dr J. Segura and Professor N. Temme for the helpful discussion on the computation of the complex Airy function. The comments by Drs Stephen Cowley and Andrew Walton and the help by Dr S. J. Leib for some of the computations are also gratefully acknowledged. Part of the work was presented by P.R. at the IUTAM Symposium on Laminar–Turbulent Transition in December 2004 in Bangalore, India, and at the 6th Euromech Fluid Mechanics Conference in June 2006 in Stockholm, Sweden.

REFERENCES

Ackerberg, R. C. & Phillips, J. H. 1972 The unsteady laminar boundary layer on a semi-infinite flat plate due to small fluctuations in the magnitude of the free-stream velocity. *J. Fluid Mech.* **51**, 137–157.

Andersson, P., Berggren, M. & Henningson, D. S. 1999 Optimal disturbances and bypass transition in boundary layers. *Phys. Fluids* **11** (1), 134–150.

Andersson, P., Brandt, L., Bottaro, A. & Henningson, D. S. 2001 On the breakdown of boundary layer streaks. *J. Fluid Mech.* **428**, 29–60.

Arnal, D. & Juillen, J. C. 1978 Contribution expérimental a l'étude de la receptivité d'une couche limite laminaire, à la turbulence de l'ecoulement general. *CERT RT 1/5018 AYD - ONERA* .

Bodonyi, R. J. & Smith, F. T. 1981 The upper branch stability of the Blasius boundary layer, including non-parallel flow effects. *Proc. R. Soc. Lond.* A **375**, 65–92.

Brandt, L., Schlatter, P. & Henningson, D. 2004 Transition in boundary layers subject to free-stream turbulence. *J. Fluid Mech.* **517**, 167–198.

Cebeci, T. 2002 *Convective Heat Transfer*. Springer.

Crow, S. C. 1966 The spanwise perturbation of two-dimensional boundary-layers. *J. Fluid Mech.* **24**, 153–164.

Demetriades, A. 1989 Growth of disturbances in a laminar boundary layer at Mach 3. *Phys. Fluids* A **1** (2), 312–317.

Dietz, A. J. 1999 Local boundary-layer receptivity to a convected free-stream disturbance. *J. Fluid Mech.* **378**, 291–317.

Dryden, H. L. 1936 Air flow in the boundary layer near a plate. *NACA Rep.* 562.

Dryden, H. L. 1955 Transition from laminar to turbulent flow at subsonic and supersonic speeds. *Conference on High-Speed Aeronautics, 41, Polytechnic of Brooklyn, New York*.

Fransson, J., Brandt, L., Talamelli, A. & Cossu, C. 2005*a* Experimental study of the stabilization of Tollmien–Schlichting waves by finite amplitude streaks. *Phys. Fluids* **17**, 054110.

Fransson, J., Matsubara, M. & Alfredsson, P. H. 2005*b* Transition induced by free-stream turbulence. *J. Fluid Mech.* **527**, 1–25.

Gil, A., Segura, J. & Temme, N. M. 2001 Computing complex Airy functions by numerical quadrature. *Modelling, Analysis and Simulation Report MAS-R0117, November 30th, 2001, Centrum voor Wiskunde en Informatica, Amsterdam.*

Goldstein, M. E. 1983 The evolution of Tollmein–Schlichting waves near a leading edge. *J. Fluid Mech.* **127**, 59–81.

Goldstein, M. E. 1997 Response of the pre-transitional laminar boundary layer to free-stream turbulence – Otto Laporte Lecture. *Bull. Am. Phys. Soc.* **42**, 2150.

Goldstein, M. E. & Hultgren, L. S. 1987 Boundary-layer receptivity to long-wave free-stream disturbances. *Annu. Rev. Fluid Mech.* **21**, 137–166.

Graziosi, P. & Brown, G. 2002 Experiments on stability and transition at Mach 3. *J. Fluid Mech.* **472**, 83–124.

Gulyaev, A., Kozlov, V., Kuzenetsov, V., Mineev, B. & Sekundov, A. 1989 Interaction of a laminar boundary layer with external turbulence. *Izv. Akad. Nauk. SSSR Mekh. Zhid. i Gaza* **6**, 700–710.

Jacobs, R. & Durbin, P. 2001 Simulation of bypass transition. *J. Fluid Mech.* **428**, 185–212.

Kemp, N. 1951 The laminar three-dimensional boundary layer and a study of the flow past a side edge. MAcs thesis, Cornell University.

Kendall, J. 1975 Wind tunnel experiments relating to supersonic and hypersonic boundary layer transition. *AIAA J.* **13**, 290–299.

Kendall, J. 1985 Experimental study of disturbances produced in a pre-transitional boundary layer. *AIAA Paper* 85-1695.

Kendall, J. 1990 Boundary layer receptivity to free stream turbulence. *AIAA Paper* 90-1504.

Kendall, J. 1991 Studies on laminar boundary layer receptivity to free-stream turbulence near a leading edge. In *Boundary Layer Stability and Transition to Turbulence* (ed. D.C. Reda, H. L. Reed & R. Kobayashi). *ASME FED* **114**, 23–30.

Klebanoff, P. 1971 Effect of free-stream turbulence on a laminar boundary layer. *Bull. Am. Phys. Soc.* **16**.

Lam, S. H. & Rott, N. 1960 Theory of linearized time-dependent boundary layers. *Cornell University Grad. School of Aero. Engineering Dept. AFOSR TN* 60-1100.

Landhal, M. 1977 Dynamics of boundary layer turbulence and the mechanism of drag reduction. *Phys. Fluids* **20** (10), 55–63.

Landhal, M. 1980 A note on an algebraic instability of inviscid parallele shear flows. *J. Fluid Mech.* **98**, 243–251.

Laufer, J. 1954 Factors affecting transition Reynolds numbers on models in supersonic wind tunnels. *J. Aero. Sci.* **21**, 497–498.

Laufer, J. 1960 Aerodynamic noise in supersonic wind tunnels. *J. Aero. Sci.* **28**, 685–692.

Leib, S. J., Wundrow, D. W. & Goldstein, M. E. 1999 Effect of free-stream turbulence and other vortical disturbances on a laminar boundary layer. *J. Fluid Mech.* **380**, 169–203.

Levin, O. & Henningson, D. S. 2003 Exponentially *vs.* algebraic growth and transition prediction in boundary layer flow. *Flow, Turbulence and Combustion* **70**, 183–210.

Luchini, P. 2000 Reynolds-number-independent instability of the boundary layer over a flat surface: optimal perturbations. *J. Fluid Mech.* **404**, 289–309.

Mack, L. 1975 Linear stability theory and the problem of supersonic boundary-layer transition. *AIAA J.* **3**, 278–289.

Mack, L. 1984 Boundary-layer linear stability theory. *Special Course on Stability and Transition of Laminar Flow. AGARD Rep.* **709**, 1–81.

Matsubara, M. & Alfredsson, P. H. 2001 Disturbance growth in boundary layers subjected to free-stream turbulence. *J. Fluid Mech.* **430**, 149–168.

Morkovin, M. 1984 Bypass transition to turbulence and research desiderata. *Transition in Turbines NASA CP* **2386**, 161–204.

Pate, S. R. 1971 Supersonic boundary-layer transition: effects of roughness and free-stream disturbances. *AIAA J.* **9**, 797–803.

Ricco, P. 2006 Response of a compressible laminar boundary layer to free-stream turbulence. PhD thesis, University of London.

Schlichting, H. 1933 Zur Entstehung der Turbulenz bei der Plattenströmung. *Math. Phys. Klasse. Nach. Ges. Wiss. Göttingen*, pp. 181–208.

Schlichting, H. & Gersten, K. 2000 *Boundary-Layer Theory*. Springer.

Schneider, S. P. 2001 Effect of high-speed tunnel noise on laminar–turbulent transition. *J. Spacecraft Rockets* **38-3**, 323–333.

Schubauer, G. & Skramstad, H. 1947 Laminar boundary-layer oscillations and transition on a flat plate. *NACA TN* **909**.

Smith, F. T. 1989 On the first-mode instability in subsonic, supersonic or hypersonic boundary layers. *J. Fluid Mech.* **198**, 127–153.

Stainback, P. 1971 Hypersonic boundary-layer transition in the presence of wind tunnel noise. *AIAA J.* **9**, 2475–2476.

Stewartson, K. 1964 *The Theory of Laminar Boundary Layers in Compressible Fluids*. Claredon.

Taylor, G. 1939 Some recent developments in the study of turbulence. *Fifth Intl Congr. for Appl. Mech.* (ed. J. P. Den Hartog & H. Peters), pp. 294–310.

Tollmien, W. 1929 Uber die Entstehung der Turbulenz 1. Mitteilung. in Math. Phys. Kl. (pp. 21–44). *Nachr. Ges. Wiss. Göttingen* (trans. into English as *NACA TM* 609 (1931)).

Westin, K., Boiko, A., Klingmann, B., Kozlov, V. & Alfredsson, P. 1994 Experiments in a boundary layer subjected to free stream turbulence. Part 1. Boundary layer structure and receptivity. *J. Fluid Mech.* **281**, 193–218.

Wu, X. 1999 Generation of Tollmien–Schlichting waves by convecting gusts interacting with sound. *J. Fluid Mech.* **397**, 285–316.

Wu, X. & Choudhari, M. 2003 Linear and non-linear instabilities of a Blasius boundary layer perturbed by streamwise vortices. Part 2. Intermittent instability induced by long-wavelength Klebanoff modes. *J. Fluid Mech.* **483**, 249–286.

Wundrow, D. W. 1996 Linear instability of a uni-directional transversely sheared mean flow. *NASA CR* 198535.

Wundrow, D. W. & Goldstein, M. E. 2001 Effect on a laminar boundary layer of small-amplitude streamwise vorticity in the upstream flow. *J. Fluid Mech.* **426**, 229–262.

Zaki, T. & Durbin, P. A. 2005 Mode interaction and the bypass route to transition. *J. Fluid Mech.* **531**, 85–111.